Investigation of the inclination angles of wall-attached eddies for streamwise velocity and temperature fields in compressible turbulent channel flows

Tianyi Bai,[1] Cheng Cheng,[1,2] and Lin Fu[1,3,4,5,*]

[1]*Department of Mechanical and Aerospace Engineering, The Hong Kong University of Science and Technology, Clear Water Bay, Kowloon, Hong Kong*

[2]*Institute for Advanced Study, The Hong Kong University of Science and Technology, Clear Water Bay, Kowloon, Hong Kong*

[3]*Department of Mathematics, The Hong Kong University of Science and Technology, Clear Water Bay, Kowloon, Hong Kong*

[4]*HKUST Shenzhen-Hong Kong Collaborative Innovation Research Institute, Futian, Shenzhen, China*

[5]*Center for Ocean Research in Hong Kong and Macau (CORE), The Hong Kong University of Science and Technology, Clear Water Bay, Kowloon, Hong Kong*

(Received 22 September 2023; accepted 22 February 2024; published 29 March 2024)

Townsend's attached eddy hypothesis (AEH), one of the most elegant models in incompressible wall turbulence, has been recently applied to compressible wall turbulence to explain the numerical observations and predict the scaling laws. Before a more profound extension can be established, a comprehensive investigation of the features of wall-attached eddies for streamwise velocity and temperature fields in compressible wall-bounded turbulence is required. In this work the AEH and the inner-outer interaction model [Marusic *et al.*, Science **329**, 193 (2010)] are combined to isolate the signature of attached eddies at a targeted length scale and then assess their inclination angles statistically based on the direct numerical simulation database. The inclination angle obtained in the streamwise velocity fluctuating fields, which approaches 45° as the Reynolds number increases, shows a minor Mach-number influence within the Mach-number range included in this work. As for those in temperature fluctuations, a high statistical similarity can be seen to streamwise velocity fluctuations. This slight Mach-number effect indicates that a uniform model can be potentially developed for compressible wall-bounded turbulence with different Mach numbers.

DOI: 10.1103/PhysRevFluids.9.034611

I. INTRODUCTION

As is well known, multiscale coherent motions, responsible for the production and dissipation of turbulence, occupy the boundary layers of wall turbulence, especially at high Reynolds numbers. Extensive studies of these motions have been conducted, and several conceptual models are developed to elucidate many prevailing features such as streaks and ejections in wall turbulence [1–3], to predict the scaling of statistics, e.g., the logarithmic behavior of the variance of streamwise velocity fluctuations [4–6] and their higher-order moments [7], and even to predict instantaneous fields and provide second-order statistics quantitatively [8–10]. One of the most successful models is the attached eddy hypothesis (AEH) [4,5] asserting that an assemble of geometrically self-similar energy-containing eddies (or coherent motions) extended to the near-wall region reside in the

*Corresponding author: linfu@ust.hk

inertial-dominated logarithmic region [11,12]. Throughout this paper, the words "motions," "structures," and "eddies" are equivalent, following the definition in Robinson [13]. From the perspective of developing turbulence models, the population, distribution, strength (vorticity), scale of attached eddies, etc., are crucial input parameters, and the streamwise inclination angle is also one of them.

The AEH empirically assumes that these motions incline downstream with an angle of approximately 45° evaluated by structures from flow visualization and vortex identification techniques [14,15]. A series of comparisons between experimental results and those of the AEH simulations [8–10] show good consistency, which seems to validate this assumption. It is also supported by theoretical estimation through the direction of the principal axis of the main strain tensor [16,17]. However, if one computes the inclination angle by means of cross-correlation of wall shear stress fluctuations (τ_w') and streamwise velocity fluctuations (u') in the logarithmic region [18], there is a conspicuous discrepancy when compared to the assumption of AEH. The cross-correlation is given by

$$R_{\tau_w' u'}(\triangle x) = \frac{\langle \tau_w'(x) u'(x + \triangle x, y_o) \rangle}{\sqrt{\langle \tau_w'^2 \rangle} \sqrt{\langle u'^2 \rangle}}, \tag{1}$$

where x denotes the streamwise direction, $\triangle x$ denotes the streamwise delay, y_o is a location in the logarithmic region, and angle brackets $\langle\rangle$ denote the ensemble time and spatial average. The inclination angle is then estimated by

$$\alpha_m = \arctan \frac{y_o}{\triangle x_p}, \tag{2}$$

where $\triangle x_p$ is the streamwise delay corresponding to the peak of $R_{\tau_w' u'}$. This method results in an inclination angle around 12°–15°, which is obviously smaller than the expected 45° of the assumption. Marusic [10] clarifies this difference by AEH simulations and predicts flow fields using an array of spatially correlated attached eddies with different scales in a similar organization to vortex packets, and all these eddies incline downstream at a constant 45°. The resultant inclination angle is similar to what is obtained in the experiment. If eddies of a specific length scale are used, the corresponding inclination angle becomes close to 45°. Therefore, the much smaller inclination angle can be attributed to the multiple scales included in the calculation of cross-correlation $R_{\tau_w' u'}$, which is a mean structure angle of different scales [10,19].

Very recently, Deshpande *et al.* [19] and Cheng *et al.* [20] proposed approaches to remove this multiscale effect. Deshpande *et al.* [19] follow the work of Baidya *et al.* [21] isolating large-scale attached structures by applying a spanwise offset between the measured field at the wall and that in the logarithmic region. They notice an inclination angle around 45°, which validates the assumption concretely. Unfortunately, their method can isolate only large-scale eddies. Cheng *et al.* [20] later develop another method based on the inner-outer interaction model (IOIM) [22] and the AEH to isolate near-wall footprints and corresponding velocity fluctuations (in the logarithmic region) of eddies at a targeted height. This approach is able to isolate eddies of a given height/scale in the logarithmic region. They report a Reynolds-number dependence of the inclination angle, which asymptotically reaches 45° as the Reynolds number increases. More details will be explained in Sec. III. These two investigations address the long-standing question about the AEH model.

While the coherent structure has been widely explored and employed for prediction in incompressible wall turbulence, only a few existing studies reveal its performance in compressible counterparts. Duan *et al.* [23] investigate the Mach-number effect by conducting direct numerical simulations (DNSs) of turbulent boundary layers with free-stream Mach numbers (M_∞) from 0.3 to 12. They report a weak compressibility influence on the streamwise extent of large-scale eddies up to $M_\infty = 3$ and a decreasing trend for higher M_∞. The structure angle is estimated by the two-dimensional contours of correlation maps given by

$$R_{(\rho u)'(\rho u)'}(\triangle x, y; \overline{y}) = \frac{\langle (\rho u)'(x + \triangle x, y)(\rho u)'(x, \overline{y}) \rangle}{\sqrt{\langle (\rho u)'^2 (x + \triangle x, y) \rangle} \sqrt{\langle (\rho u)'^2 (x, \overline{y}) \rangle}}, \tag{3}$$

where ρ is density and $\overline{y}$ is a reference wall-normal location around which the correlation is computed. For a specific $\overline{y}(\overline{y}/\delta = 0.2$ in Duan *et al.* [23]), y varies to attain a two-dimensional contour of the correlation map with $\triangle x$ for the abscissa and y for the ordinate. The angle of the structure is observed to remain similar for $M_\infty < 3$. Pirozzoli and Bernardini [24] carry out DNSs of turbulent boundary layers at $M_\infty = 2$. Similar to incompressible flows, the streamwise and spanwise velocity variance shows a logarithmic decay, indicating an attached feature, while the wall-normal velocity is detached. Pirozzoli and Bernardini [24] also conclude that thermal properties, such as pressure, density, and temperature, are all attached variables. As observed by Duan *et al.* [23], the length scales of eddies agree with the incompressible cases at a similar Reynolds number. Pirozzoli and Bernardini [24] apply one extra step than Duan *et al.* [23], i.e., a linear least-square fit to the correlation maps of u' in order to quantify the structure angle (see Figs. 22 and 23 in Pirozzoli and Bernardini [24]). In the outer region, they attain an angle close to the Reynolds-number-invariant structure angle of large-scale attached eddies in incompressible regime (14°) [18]. The angles of ρ- and T-bearing eddies are examined as well. The ρ-bearing eddies have the steepest inclination angle, and those of T-bearing eddies are double or triple those of u-bearing eddies. Overall, contrary to some early experiments claiming an obvious distinction of structure scales between compressible and incompressible flows [25–28], most scrutinies of DNSs support the conclusion that at moderate Mach numbers, the structure similarity between compressible and incompressible flows can be expected. The structures in velocity and temperature fields can also be estimated by linear models (stochastically forced linearized equations) as claimed by Chen *et al.* [29]. Although these studies mentioned above go beyond the explicit study of attached eddies, they could potentially be a reference for this work as well.

Specifically for the AEH, Yu *et al.* [30] decompose the spectra into wall-attached (WA) and wall-detached (WD) portions by the proper orthogonal decomposition to analyze the statistics of velocity and temperature fields in compressible channel flows. They observe a high similarity of the spectra and variances between temperature and velocity fluctuations. Cheng and Fu [31] confirm the existence of wall-attached self-similar structures by the linear coherence spectrum in streamwise velocity and temperature fluctuations of compressible channel flows. They both have a similar streamwise/wall-normal aspect ratio of 15.5, consistent with the value 14 in incompressible flows reported by Baars *et al.* [32]. One can see that the existence of attached eddies in compressible flows has been preliminarily shown. Nevertheless, many features of attached eddies remain unclear, e.g., their strength, population, and the inclination angle discussed above. This work is dedicated to investigating the Mach-number effect on the streamwise inclination angle of wall-attached eddies in compressible channel flows using the database from DNSs. The temperature fluctuation field is also taken into account to characterize features of its WA portion. The studies of these characteristics help to establish the foundation to extend the incompressible AEH to compressible flows such that the AEH can be employed to predict the scaling of statistics and reconstruct instantaneous fields for both the streamwise velocity and temperature of compressible flows. The analysis of turbulent structures can also benefit the development of near-wall models [33,34].

This work is organized as follows. Section II summarizes briefly the DNS database for compressible channel flows examined in this paper. The methodology to isolate eddies of a given scale is illustrated in Sec. III. We present the main results and discussions in Sec. IV. Finally, Sec. V provides the conclusion.

II. DNS DATABASES AND JARGON INTERPRETATIONS

Five compressible channel flow cases are considered in this work with some of their parameters listed in Table I. The accuracy of the four DNS results with $\mathrm{Ma}_b \leqslant 1.5$ has been validated in [31]. Appendix A shows the accuracy of the DNS at $\mathrm{Ma}_b = 3$. It should be noted that this is the highest Mach number we simulate within our capability. In the forthcoming discussion, the streamwise direction is designated by the x coordinate, the wall-normal direction by the y coordinate, and the spanwise direction by the z coordinate. h is half of the channel height. Variables are composited by

TABLE I. Numerical parameters for DNSs of channel flows employed in this work. Re_τ is the friction Reynolds number; Re_τ^* the semilocal friction Reynolds number. These cases are named according to their bulk Mach numbers (see more details in [31]). The last row shows colors and line styles used to distinguish them.

Case	M08R8K	M08R17K	M15R9K	M15R20K	M30R15K
Re_τ	443	893	598	1167	1243
Re_τ^*	381	778	393	770	396
Ma_b	0.8	0.8	1.5	1.5	3.0
Label	– – – – –	....	– – – – –	....	– – – – –

either the Reynolds ($\phi = \overline{\phi} + \phi'$) or Favre ($\phi = \widetilde{\phi} + \phi''$) decomposition, where $\overline{\phi}$ and $\widetilde{\phi} = \overline{\rho\phi}/\overline{\rho}$ denote the averaged portion, and ϕ' and ϕ'' denote the fluctuating portion, respectively. Variables in wall units are distinguished by the plus sign superscript, and those in semilocal units by the asterisk superscript. The wall units comprise the friction velocity $u_\tau = \sqrt{\tau_w/\overline{\rho}_w}$ and the viscous length scale $\delta_\tau = \overline{\mu}_w/(u_\tau\overline{\rho}_w)$, where ρ_w is the density at the wall, μ_w is the viscosity at the wall, and $\tau_w = \overline{\mu}_w(\partial\widetilde{u}/\partial y)|_w$ is the wall shear stress. Here are examples of variables in wall units, $\widetilde{u}^+ = \widetilde{u}/u_\tau$, $y^+ = y/\delta_v$, $\overline{\mu}^+ = \overline{\mu}/\overline{\mu}_w$, $\overline{\rho}^+ = \overline{\rho}/\overline{\rho}_w$. The characteristic Reynolds number for turbulent channel flows is the friction Reynolds number defined as $\mathrm{Re}_\tau = \rho_w u_\tau h/\mu_w$. As for variables in semilocal units, the velocity scale is $u_\tau^* = \sqrt{\tau_w/\overline{\rho}}$ and the length scale is $\delta_\tau^* = \overline{\mu}/(u_\tau^*\overline{\rho})$. $\mathrm{Re}_\tau^* = \rho_c\sqrt{\tau_w/\rho_c}h/\mu_c$ is the semilocal counterpart of the friction Reynolds number, where ρ_c is the density and μ_c is the dynamic viscosity at the center line of the channel. This work concentrates on the logarithmic region defined as $y^* > 100$ and $y/h < 0.3$, and $y/h > 0.3$ is designated as the outer region.

III. LINEAR SYSTEMS AND ISOLATION OF EDDIES

According to the AEH [4], the very-large-scale motions (VLSMs) centering in the logarithmic and outer regions extend down to the wall, superimpose their signature, and modulate the small-scale fluctuations in the near-wall region [22]. To extract the wall-coherent large-scale and very-large-scale portion, the velocity and temperature fluctuations are analyzed and predicted via spectral linear stochastic estimation (SLSE), a well-established method in the linear system theory [35]. A brief introduction and explanation of the linear system theory and SLSE are provided in Sec. III A; Sec. III B clarifies the methodology to isolate the signature of attached eddies of a selected scale, and Sec. III C computes the corresponding streamwise inclination angle.

A. Linear systems and spectral linear stochastic estimation

A single-input/single-output constant-parameter linear system has an input $x(t)$, an output $y(t)$, and a time-invariant dynamic characteristic described by the impulse response function $h(\tau)$ [35]. $h(\tau)$ is the system output responding to a unit impulse at a time τ before. The output $y(t)$ at any time t is a linear sum of the entire history of the input $x(t)$ weighted by the impulse response function $h(\tau)$ given by the convolution integral

$$y(t) = \int_{-\infty}^{+\infty} h(\tau)x(t-\tau)\,d\tau. \tag{4}$$

By applying the Fourier transform to both sides of Eq. (4), one obtains its spectral features

$$Y(f) = H(f)X(f), \tag{5}$$

where $Y(f)$, $X(f)$, and $H(f)$ are the Fourier transform of $y(t)$, $x(t)$, and $h(t)$, respectively. Equation (5) is referred to as the spectral linear stochastic estimation if $H(f)$ is a linear kernel. Once the transfer kernel $H(f)$ is solved, an estimation of the output $y(t)$ for a given input $x(t)$ can be done.

The transfer kernel, also named the frequency response function $H(f)$, is estimated in the least square sense. In short, the mean square of the error, i.e., the difference between the estimated output $\hat{y}(t)$ and the measured one $y(t)$, is minimized over all $H(f)$, and the first derivative of the mean square error with respect to $H(f)$ is zero. The rigorous derivation can be found in [35,36]. This $H(f)$ is shown to be

$$H(f) = \frac{\langle \overline{X(f)} Y(f) \rangle}{\langle \overline{X(f)} X(f) \rangle}, \tag{6}$$

where $\overline{X(f)}$ is the complex conjugate of $X(f)$. The transfer kernel $H(\lambda_x)$ is a function of frequency or wavelength in our application only. It indicates that there is no frequency (wavelength) translation in this linear system, and a much simpler interpretation can be found in the Fourier space than in the physical domain. The transfer kernel $H(f)$ can be divided into two parts, namely,

$$H(f) = |H(f)| e^{i\phi(f)}, \tag{7}$$

where the modulus $|H(f)|$ is the gain factor, $||$ is the modulus of complex numbers, $\phi(f)$ is the phase factor, and $i^2 = -1$.

The applicability of SLSE is examined by the linear coherence function (LCF) $\gamma^2(f)$ defined as

$$\gamma^2(f) = \frac{|\langle \overline{X(f)} Y(f) \rangle|^2}{\langle |X(f)|^2 \rangle \langle |Y(f)|^2 \rangle}. \tag{8}$$

In Eq. (8) the numerator is the squared cross-spectral density function and the denominator is the product of autospectral density functions of the input x and the output y. $\gamma^2(f)$ is analogous to the square cross-correlation coefficient function $R_{\tau_w' u'}(\triangle x)$ in Eq. (1) replacing the streamwise distance with wavelength as the independent variable, which implies the linear coherence between the input and output at a specific wavelength λ_x.

Although the input and output examples in the above illustration are defined as functions of time, other parameters, such as streamwise distance (x), can supplant time as the independent variable. In the forthcoming discussion, we replace t with x. Subsequently, in the Fourier space, frequency f is replaced by wave number ω or wavelength λ_x. According to the IOIM [22], Baars *et al.* [37] estimate the near-wall footprint of VLSM based on the linear system theory using the transfer kernel in Eq. (6), which provides a promising result. Later Cheng and Fu [38], following the IOIM [22], adopt this kernel to predict the streamwise wall-shear stress fluctuations by the signal of streamwise velocity fluctuation in the logarithmic region. They subtract two predictions from two neighboring wall-normal positions to isolate the contribution from attached eddies whose heights reside within these two neighbors and assert that the superposition effects from attached eddies follow a strict additive process. Besides the prediction of the inner region from the outer region, it can also be used to estimate streamwise velocity fluctuations in the logarithmic region by their near-wall counterparts [20] and inspect the multiphysics couplings in compressible flows [39]. Thus, the reliability of this method has been widely verified.

B. Isolation of attached eddies

As discussed in the preceding section, SLSE could offer a reliable prediction of velocity fields in the near-wall region and the logarithmic region to identify the signature of attached eddies. In short, if we simplify IOIM [22] by ignoring the modulation process, the near-wall signal can be expressed by $u_i'' = u_{i,fp}'' + u_{i,un}''$, where $u_{i,fp}''$ and $u_{i,un}''$ are the footprints of large-scale attached eddies and the universal component, respectively. $u_{i,un}''$ is assumed to be uncorrelated with $u_{i,fp}''$ and u_o''. The imposed large-scale influence ($u_{i,fp}''$), can be estimated by streamwise velocity fluctuations in the logarithmic region $u_o''(y_o)$ using SLSE, i.e., $u_{i,L}''$ given by Eq. (9), where the subscript i indicates that it is in the inner layer y_i and L means the contribution from large-scale motions [22,37]. This

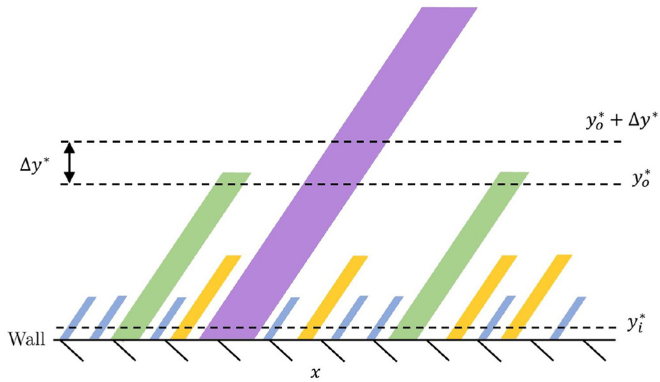

FIG. 1. Schematic diagram of a hierarchy of self-similar attached eddies in the x-y plane. Four hierarchy levels are included and represented by trapezoids with different colors: the smallest eddies are in blue, and the highest ones are in purple. y_i^* is the wall-normal distance of the grids adjacent to the wall. y_o^* represents the wall-normal distance in the logarithmic region, and $y_o^* + \triangle y^*$ is the neighbor location of y_o^* with a distance $\triangle y^*$, which is also in the logarithmic region.

section emphasizes the methodology to isolate the signature of attached eddies with a given scale [20,40].

Figure 1 shows a sketch considering the volume of influence for a hierarchy of self-similar attached eddies. Four hierarchy levels are characterized by trapezoids with different colors. From the smallest attached eddies in blue, their higher consecutive hierarchy has a doubled eddy size and a halved number density as indicated in Fig. 1. The AEH assumes no interaction between attached eddies at different length scales, and the contribution from all attached eddies follows a simple linear superposition. One can, consequently, deduce that the streamwise velocity fluctuation at y_o^* (the subscript o designates the quantity in the logarithmic region) includes the signatures of attached eddies higher than y_o^*. Equipped with SLSE and the AEH, we are ready to isolate the signature of attached eddies at a given height or scale.

For compressible flows, the density-weighted velocity fluctuation $\sqrt{\rho}u''$ instead of u'' is supposed to be employed to account for the density variation [39] according to Morkovin's hypothesis [41]. In this work, we designate the density-weighted velocity fluctuation, $\sqrt{\rho}u''$, as u''', and $u'''^+ = \overline{\sqrt{\rho}u''}/(u_\tau\sqrt{\rho_w})$. It is worthwhile to note that the authors do not notice a significant difference in the inclination angle using velocity fluctuations with and without the weight by density. The corresponding equation is given by

$$u'''_{i,L}(x, y_o^*) = F_x^{-1}\{H_L(\lambda_x, y_o^*)U_o(\lambda_x, y_o^*)\}, \tag{9}$$

where F_x^{-1} is the inverse Fourier transform operator in the streamwise direction, $U_o(\lambda_x, y_o^*) = F_x\{u_o'''(x, y_o^*)\}$, F_x is the Fourier transform operator in the streamwise direction, and λ_x is the streamwise wavelength. When conducting such estimation, the transfer kernel is set to be zero for $\lambda_x^+ < 700$ to further eliminate the small-scale influence. The transfer kernel $H_L(\lambda_x, y_o^*)$ is equivalent to the one defined in Eq. (6), namely, defined as

$$H_L(\lambda_x, y_o^*) = \frac{\langle\overline{U_o(\lambda_x, y_o^*)}U_i(\lambda_x, y_i^*)\rangle}{\langle\overline{U_o(\lambda_x, y_o^*)}U_o(\lambda_x, y_o^*)\rangle}, \tag{10}$$

where $U_i(\lambda_x, y_i^*) = F_x\{u_i'''(x, y_i^*)\}$ is the Fourier transform of the streamwise velocity fluctuation $u_i'''(x, y_i^*)$ at y_i^*. $u'''_{i,L}(x, y_o^*)$ obtained by Eq. (9) records the signature of attached eddies higher than y_o^*, since the transfer kernel $H_L(\lambda_x, y_o^*)$ characterizes coherent features between the near-wall position y_i^* and y_o^* in the logarithmic region. Similarly, we can replace y_o^* in Eq. (9) by $y_o^* + \triangle y^*$ to compute

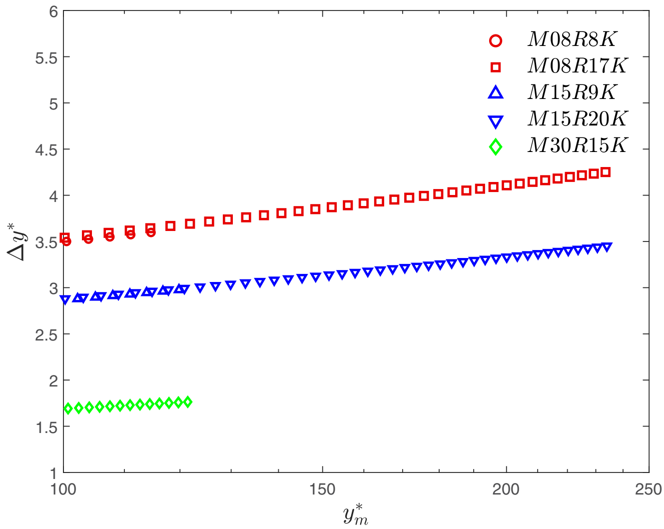

FIG. 2. Distance $\triangle y^*$ between two neighbor grids y_o^* and $y_o^* + \triangle y^*$ in the wall-normal direction as a function of estimated eddy height $y_m^* = (y_o^* + y_o^* + \triangle y^*)/2$.

the signature $u'''_{i,L}(x, y_o^* + \triangle y^*)$ of attached eddies higher than $y_o^* + \triangle y^*$ at y_i^*. Then a subtraction,

$$\triangle u'''_{i,L}(x, y_o^*) = u'''_{i,L}(x, y_o^*) - u'''_{i,L}(x, y_o^* + \triangle y^*), \tag{11}$$

is needed to identify the signature induced by attached eddies whose heights lie between y_o^* and $y_o^* + \triangle y^*$, due to the linear superposition assumption of the AEH [4]. Figure 1 demonstrates this point clearly. If we apply this methodology to the hierarchy of attached eddies shown in Fig. 1, $u'''_{i,L}(x, y_o^*)$ contains signatures of the third (green) and fourth (purple) hierarchy levels, and only the fourth level contributes to $u'''_{i,L}(x, y_o^* + \triangle y^*)$. It is obvious that $\triangle u'''_{i,L}(x, y_o^*)$ records merely the third level. Even though Fig. 1 uses eddies of discrete scales, it can be representative of the continuous scale of the attached eddies in the real turbulent field to a large extent. This step also requires $\triangle y^* \ll y_o^*$ such that attached eddies residing between y_o^* and $y_o^* + \triangle y^*$ are considered to be of the same scale approximately $y_m^* = (y_o^* + y_o^* + \triangle y^*)/2$. It is verified in Fig. 2 that all the cases have a maximum $\triangle y^* < 4.5$.

Equivalently, velocity fluctuations at y_o^* can also be estimated by those at y_i^*. Commuting $u_i'''(x, y_i^*)$ and $u_o'''(x, y_o^*)$, Eq. (9) now becomes

$$u'''_{o,W}(x, y_o^*) = F_x^{-1}\{H_W(\lambda_x, y_o^*)U_i(\lambda_x, y_i^*)\}, \tag{12}$$

and the corresponding $H_W(\lambda_x, y_o^*)$ is

$$H_W(\lambda_x, y_o^*) = \frac{\langle \overline{U_i(\lambda_x, y_i^*)} U_o(\lambda_x, y_o^*)\rangle}{\langle \overline{U_i(\lambda_x, y_i^*)} U_i(\lambda_x, y_i^*)\rangle}. \tag{13}$$

$u'''_{o,W}(x, y_o^*)$ is wall-coherent signatures from eddies higher than y_o^* at y_o^* (the signatures of eddies in the third and fourth hierarchy levels in Fig. 1 at y_o^*). Replacing y_o^* by $y_o^* + \triangle y^*$, the obtained $u'''_{o,W}(x, y_o^* + \triangle y^*)$ represents signatures from eddies higher than $y_o^* + \triangle y^*$ at $y_o^* + \triangle y^*$ (the signatures of eddies in the fourth hierarchy level only in Fig. 1 at $y_o^* + \triangle y^*$). The subtraction,

$$\triangle u'''_{o,W}(x, y_m^*) = u'''_{o,W}(x, y_o^*) - u'''_{o,W}(x, y_o^* + \triangle y^*), \tag{14}$$

helps identify the contribution by attached eddies locating between y_o^* and $y_o^* + \triangle y^*$ (eddies in the third hierarchy levels in Fig. 1). The signal $\triangle u'''_{o,W}(x, y_m^*)$ itself is in the logarithmic region, and the height (scale) of attached eddies contributing to it is estimated by $y_m^* = [y_o^* + (y_o^* + \triangle y^*)]/2$.

C. Streamwise inclination angle of eddies of a given scale

Noting that the signature of eddies at a given scale is isolated, one can then determine the corresponding streamwise inclination angle through the cross-correlation following the traditional way,

$$R_{\triangle\tau'''_{w,L}\triangle u'''_{o,W}}(\triangle x^*) = \frac{\triangle\tau'''_{w,L}(x^*)\triangle u'''_{o,W}(x^* + \triangle x^*, y^*_m)\rangle}{\sqrt{\langle \triangle\tau'''_{w,L}{}^2\rangle}\sqrt{\langle \triangle u'''_{o,W}{}^2\rangle}} \tag{15}$$

and

$$\alpha_s(y^*_m) = \arctan\frac{y^*_m}{\triangle x^*_p}, \tag{16}$$

where the wall-shear stress is evaluated by $\triangle\tau'''_{w,L}(x^*) = \partial\triangle u'''_{i,L}(x^*, y^*_o)/\partial y^*$, and $\triangle x^*_p$ is the streamwise delay corresponding to the peak of $R_{\triangle\tau'''_{w,L}\triangle u'''_{o,W}}(\triangle x^*)$. $\alpha_s(y^*_m)$ is the streamwise inclination angle of eddies with the height y^*_m, which is different from the traditional one α_m in Eq. (2). α_s is supposed to be 45° for high-Reynolds-number wall turbulence based on the AEH [4]. As for temperature fluctuations, the same procedure as streamwise velocity fluctuations can be conducted with the wall shear stress τ'''_w replaced by the wall heat flux q_w and u''' replaced by T'.

IV. RESULTS AND DISCUSSIONS

This section validates the methodology in Sec. III based on the compressible DNS data. Section IV A shows the applicability of SLSE through LCF defined in Eq. (8) indicating the correlation degree of the input and output. The spectrum properties of transfer kernel and the isolated signatures of attached eddies of height approximately y^*_m will be discussed in Sec. IV B, and conditional statistics of extracted attached eddy signatures, such as scale and intensity, are examined in Sec. IV C, which verifies the methodology and the related assumptions in Sec. III. Section IV D analyzes the Mach-number impact on the streamwise inclination angle α_s for attached eddies at a given height or scale, and shows its comparison with the traditional one α_m (in the mean sense).

A. Linear coherence function

The applicability of SLSE is examined by LCF, $\gamma^2(\lambda^+_x)$ defined in Eq. (8), the numerator is the squared cross-spectral density function, and the denominator is the product of autospectral density functions of u'''_o and u'''_i. $\gamma^2(\lambda^+_x)$ is analogous to the square cross-correlation coefficient function $R_{\tau'_w u'}(\triangle x)$ in Eq. (1) replacing the streamwise distance with wavelength as the independent variable, which implies the linear coherence between the input and output at a specific wavelength λ^+_x.

Figures 3 and 4 present contours of the LCF, $\gamma^2(\lambda^+_x)$ of streamwise velocity u''' and temperature T' fields, respectively. The $\gamma^2(\lambda^+_x)$ contours of the temperature share an identical feature with that of streamwise velocity. It is unsurprising that the strong Reynolds analogy (SRA) has been established in compressible wall-bounded turbulent flows [24,42,43], indicating that the temperature field performs more like a passive scalar transported by the velocity fields. This observation of similar LCF contours provides further evidence for the strong analogy between temperature and velocity fields. The LCF is determined by the ratio between the wall-coherent portion and the residual of the output and input. Thus, this similarity of LCF implies that the temperature and streamwise velocity fluctuations share a similar percentage of energy contributed by wall-attached eddies. The hierarchical self-similarity of attached eddies leads to the triangle region with sides in black dotted lines [32], and the contour is supposed to align with the hypotenuse within this region. The hypotenuse is $\lambda_x/y = 14$, where 14 is the streamwise/wall-normal aspect ratio determined from incompressible flows [32]. The lower side is $y^* = 100$, indicating the beginning of the logarithmic region. The right side $\lambda_x/h = 10$ is the outer scaling limit of the self-similar structures, after which the scale-independence trend of γ^2 should appear. The scaling independence of γ^2 is not observed in

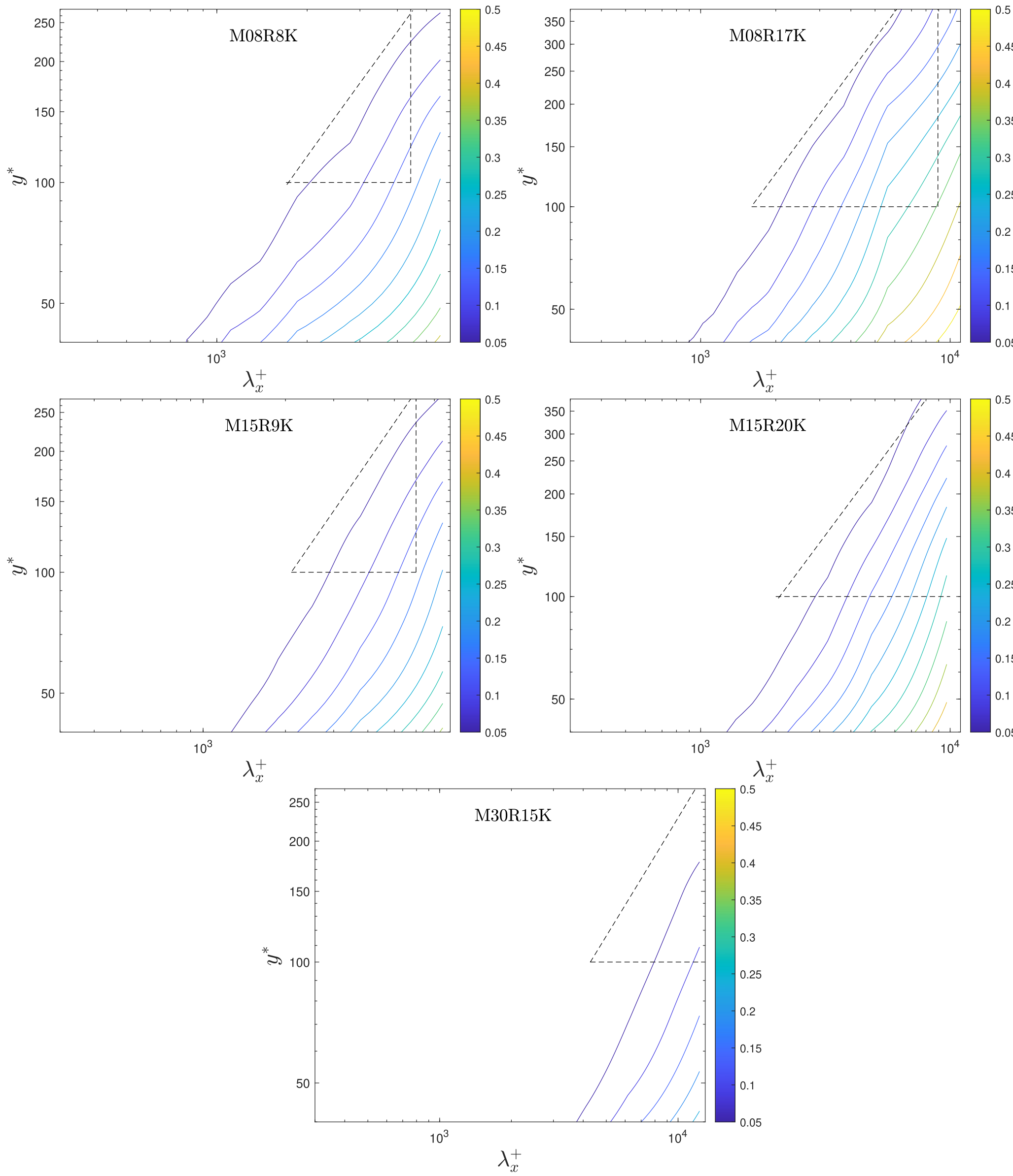

FIG. 3. Contours of LCF, $\gamma^2(\lambda_x^+)$ as a function of the wall-normal distance y^* and wavelength λ_x^+ computed from the streamwise velocity fluctuating u'' field in Table I. $\gamma^2(\lambda_x^+)$ represents the coherent degree of streamwise velocity fluctuations near the wall and at y^* (the y coordinate in the figure) in the logarithmic region. Black dotted lines indicate the region bounded by $y^* > 100$, $\lambda_x/h = 10$, and $\lambda_x/y = 14$, which is supposed to show the self-similar property of attached eddies [32].

this work due to the confined size of computation domains, and the right side is not plotted for cases M15R20K and M30R15K for the same reason. In Figs. 3 and 4, the contours of γ^2 are not exactly parallel to the hypotenuse. This tendency appears in both the streamwise velocity and temperature fields, and high-Mach-number cases may have a more obvious deviation. Results from higher Mach numbers are required to further verify it. Nevertheless, the LCF of compressible flows is roughly consistent with incompressible wall turbulence for the considered DNS data.

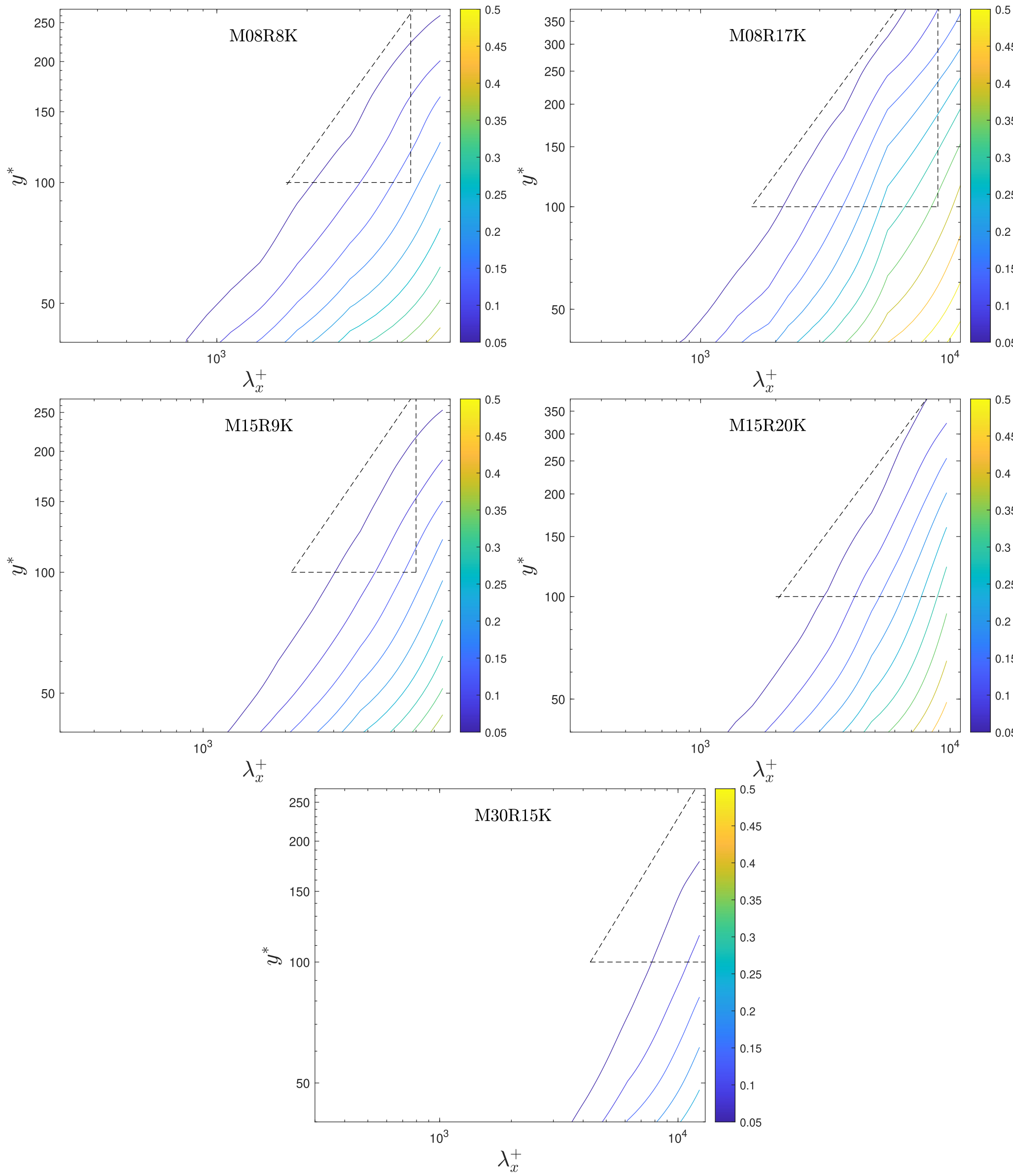

FIG. 4. Contours of LCF, $\gamma^2(\lambda_x^+)$ as a function of the wall-normal distance y^* and wavelength λ_x^+ computed from the temperature fluctuating T' field in Table I. $\gamma^2(\lambda_x^+)$ represents the coherent degree of streamwise velocity fluctuations near the wall and at y^* (the y coordinate in the figure) in the logarithmic region. Black dotted lines indicate the region bounded by $y^* = 100$, $\lambda_x/h = 10$, and $\lambda_x/y = 14$, which is supposed to show the self-similar property of attached eddies [32].

The existence of the self-similar wall-attached structure in both the streamwise velocity and temperature fields has been confirmed in Figs. 3 and 4. This conclusion allows us to extend the AEH [4] of incompressible flows to compressible wall-bounded flows. Hence, the methodology developed for incompressible flows in Sec. III is applicable to this study on compressible flows, and the investigation of the structure inclination angle is meaningful as an essential parameter for the AEH [4].

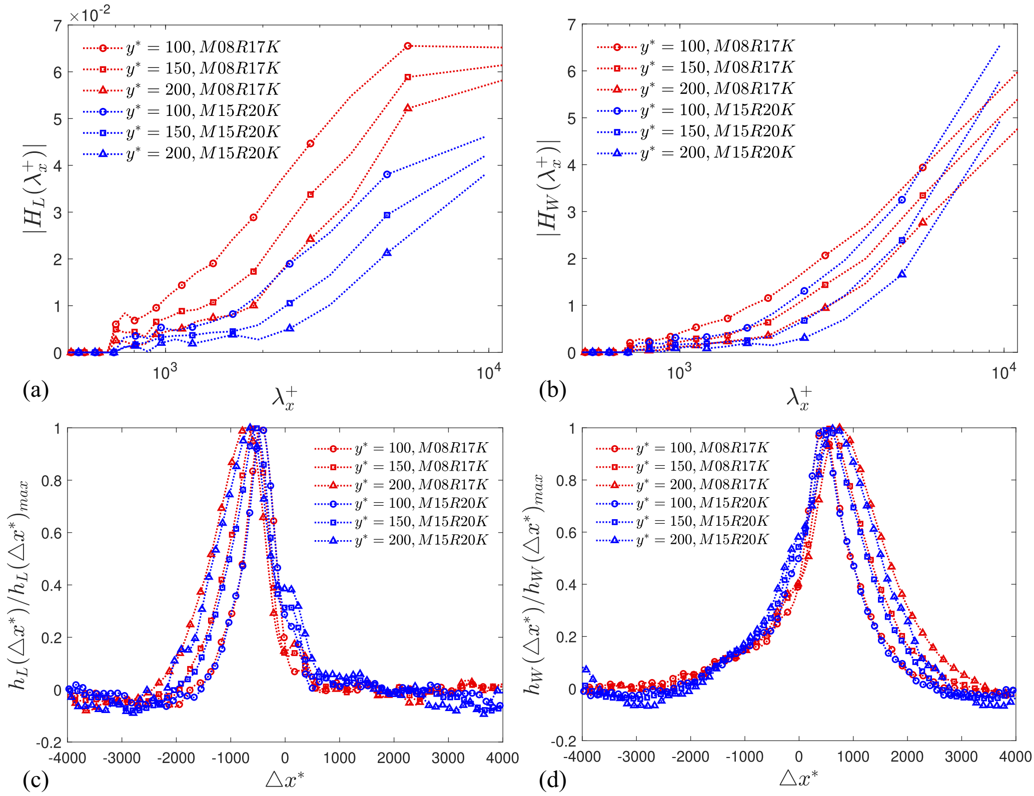

FIG. 5. Gain factor with respect to the wavelength λ_x^+ and the corresponding impulse response function $h(\triangle x^*) = F_x^{-1}(H(\lambda_x^+))$ normalized by its maximum $h(\triangle x^*)/h(\triangle x^*)_{\max}$ at three selected wall-normal positions $y^* \approx 100$, 150, and 200 computed from the streamwise velocity fluctuating u''' field for the two highest Reynolds-number cases in Table I. (a) $|H_L(\lambda_x^+)|$ and (c) the normalized $h_L(\triangle x^*)$, which are imposed on velocity fluctuations in the logarithmic region to estimate the near-wall footprint; (b) $|H_W(\lambda_x^+)|$ and (d) the normalized $h_W(\triangle x^*)$, which are imposed on near-wall velocity fluctuations to predict those in the logarithmic region.

B. Spectrum features related to attached eddies

Now that we have shown that SLSE is applicable, it is time to examine its properties in the Fourier space before the estimation. We will see how the estimation is done in both the Fourier and physical domains and the energy spectra before and after applying the scale-separation technique to inspect its effectiveness.

The gain factors at three specific wall-normal distances ($y^* \approx 100$, 150, and 200) are plotted versus λ_x^+ for the streamwise velocity u''' and temperature fluctuation T' in Figs. 5 and 6(a), respectively. The gain factor $|H_L(\lambda_x^+)|$ is exerted on the fluctuating fields in the logarithmic region to predict its near-wall influence. Although $|H_L(\lambda_x^+)|$ increases as the wavelength grows, i.e., more energy of large-scale eddies is retained, it is, overall, much smaller than unity as shown in Figs. 5 and 6(a), especially for the velocity fluctuation. This observation can be mainly attributed to the relatively lower Reynolds number where attached eddies are less populated, since for high Reynolds-number scenarios, $|H_L(\lambda_x^+)|$ reaches a plateau at around 0.6 in incompressible wall turbulence [37]. During the estimation, a significant shrink of energy contained in each Fourier mode is required. Also worth mentioning is that unlike the similarity between velocity and temperature fluctuations noticed in LCF, $|H_L(\lambda_x^+)|$ for T'^+ is nearly four times larger than that of u'''.

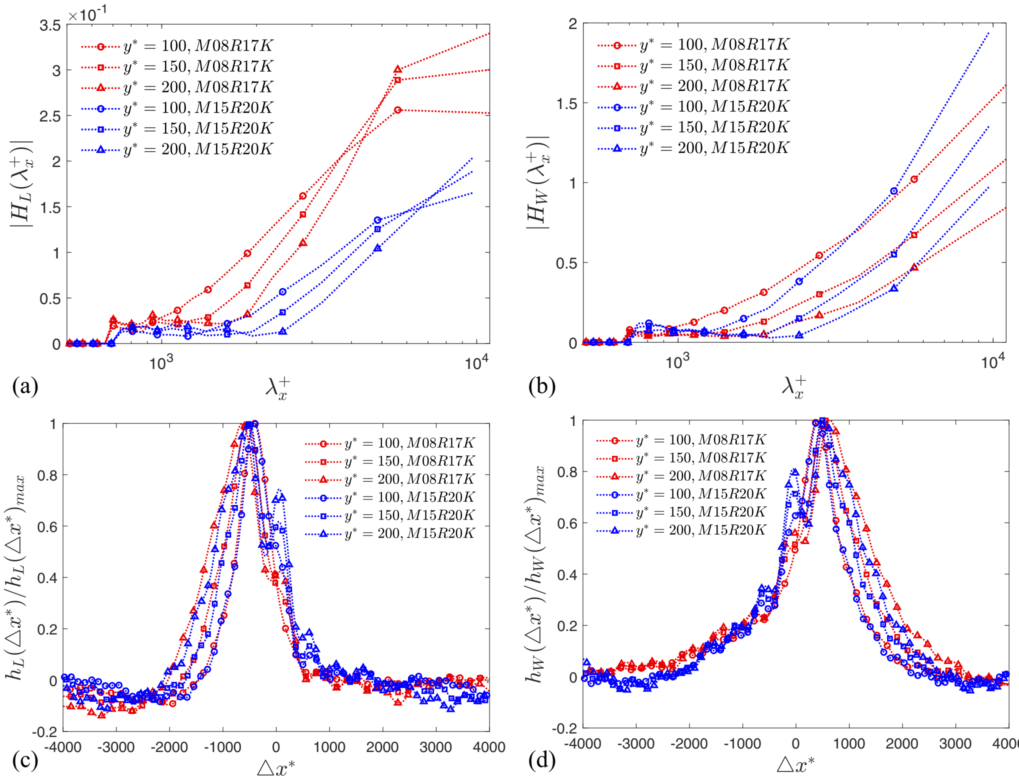

FIG. 6. Gain factor with respect to the wavelength λ_x^+ and the corresponding impulse response function $h(\triangle x^*) = F_x^{-1}(H(\lambda_x^+))$ normalized by its maximum $h(\triangle x^*)/h(\triangle x^*)_{\max}$ at three selected wall-normal positions $y^* \approx 100$, 150, and 200 computed from the temperature fluctuating T' field for the two highest Reynolds-number cases in Table I. (a) $|H_L(\lambda_x^+)|$ and (c) the normalized $h_L(\triangle x^*)$, which is imposed on velocity fluctuations in the logarithmic region to estimate the near-wall footprint; (b) $|H_W(\lambda_x^+)|$ and (d) the normalized $h_W(\triangle x^*)$, which are imposed on near-wall velocity fluctuations to predict those in the logarithmic region.

$|H_W(\lambda_x^+)|$, imposed on the near-wall fluctuations, is supposed to be larger than unity as a reciprocal of $|H_L(\lambda_x^+)|$ for ideal linear systems. However, $|H_W(\lambda_x^+)| < 1$ exists for a shorter wavelength, especially in temperature fields as demonstrated in Figs. 5 and 6(b). This is due to the universal signal of the near-wall region and the wall-detached portion in the logarithmic region. The transfer kernels utilized in this work are merely an optimum approximation of the exact ones. The decomposition of the signal into wall-coherent portions and the universal/wall-detached parties is always helpful. As obtained in Appendix B, Eq. (B1) manifests that the gain factor of the practical transfer kernel is smaller than that of the exact one. Again, the inconsistency between velocity and temperature fluctuations appears, i.e., $|H_W(\lambda_x^+)|$ for T' becomes less than that of u'''. A much larger energy discrepancy of each Fourier mode also shows for streamwise fluctuating velocity compared with the temperature fluctuations. This difference seems to challenge the SRA since distinguishing transfer kernels, which characterize the interaction between the inner and outer regions, are inspected for the temperature and velocity field, and this requires further investigation.

The normalized impulse response function $h_L(\triangle x^*)/h_L(\triangle x^*)_{\max}$ and $h_W(\triangle x^*)/h_W(\triangle x^*)_{\max}$ [Figs. 5 and 6(c) and 6(d)], defined as the inverse Fourier transform of $H_L(\lambda_x^+)$ and $H_W(\lambda_x^+)$, respectively, illustrates the dependence of output signals on its upstream and downstream information in physical domain. Since panels (c) and (d) carry similar information, hereafter, the discussion concentrates on h_L, i.e., panel (c). Recalling Eq. (4), $h_L(\triangle x^*)$ and $h_W(\triangle x^*)$ are weighting factors

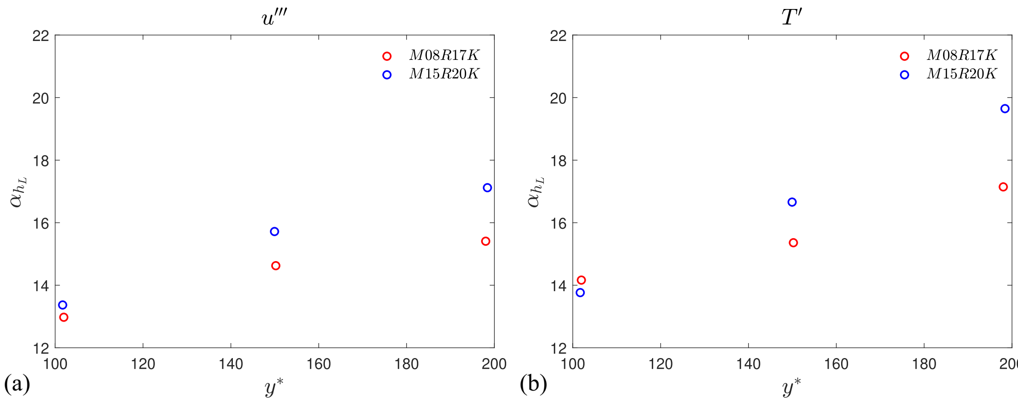

FIG. 7. Streamwise inclination angles α_{h_L} defined by Eq. (17) computed based on the peak of the impulse response function h_L at three selected wall-normal positions $y^* \approx 100$, 150, and 200 using the two highest Reynolds-number cases in Table I. (a) α_{h_L} in streamwise velocity fluctuations u'''; (b) the same in temperature fluctuations T'.

imposed on the input signal u''' at a specific location $x^*_{\text{output}} - \triangle x^*$, where the x^*_{output} is the location of the estimated output. The product $h_L(\triangle x^*)u(x^*_{\text{output}} - \triangle x^*)$ evaluated the contribution of the input $u'''(x^*_{\text{output}} - \triangle x^*)$ to the predicted output, and the integration in Eq. (4) represents a summation of contributions from the overall input (input signal at all available locations). Therefore, the scenario $\triangle x^* < 0$ implies the weighting function of its downstream information, and $\triangle x^* > 0$ is for upstream information. In Fig. 5(c), $h_L(\triangle x^*)/h_L(\triangle x^*)_{\max} \neq 0$ falls primarily into the region $\triangle x < 0$. It indicated that the estimated near-wall u'''_i depends mainly on the downstream portion of the input u'''_o in the logarithmic region, which is consistent with AEH as attached eddies are supposed to lean downstream. To further quantify its downstream dependence, we define another streamwise inclination angle α_{h_L}, namely,

$$\alpha_{h_L} = \arctan \frac{y^*_o}{\triangle x^*_{p,h}}, \tag{17}$$

where $\triangle x^*_{p,h}$ is the streamwise location corresponding to the peak value of $h_L(\triangle x^*)_{\max}$. α_{h_L} of the velocity fluctuating field is plotted in Fig. 7(a), which is $13^\circ - 17^\circ$. This newly defined inclination angle agrees with that in earlier studies [18], i.e., the mean structure inclination angle of multiple scales, for the reason that α_{h_L} is affected by all attached eddies higher than the wall-normal distance of the input position. It is now reasonable to conclude that $h_L(\triangle x^*/h_L(\triangle x^*)_{\max} \neq 0$ in $\triangle x^* < 0$ is a typical feature of the AEH [4]. This symbolic feature is also noticed in temperature fluctuating fields in Fig. 7(b). α_{h_L} of temperature fluctuations is $14^\circ - 20^\circ$. The slightly higher inclination angle of temperature fluctuations might be attributed to its more passive dynamics, which is also detected by Pirozzoli and Bernardini [24]. In short, both the wall coherent portions of the streamwise velocity and temperature fluctuations are dominated by attached eddies inclining downstream (the AEH [4]) as indicated by α_{h_L} in Fig. 7, supporting the SRA in compressible wall-bounded turbulence.

A close examination of the spectral property is required to further validate the methodology in Sec. III B. Figure 8 exhibits premultiplied spectra of streamwise velocity and temperature fluctuations before and after implementing the scale-separation methodology of attached eddies. The lines in red are the original premultiplied spectra, while those in black are from eddies of a given scale. Figures 8(a) and 8(b) plots the premultiplied spectra, and those with small magnitudes are amplified by a factor clarified in the legend. It is evident that the spectra become much smaller than the original one after conducting the scale separation step as the scale separation methodology extracts a subset of the original one contributed from the attached eddies. In order to examine the relative

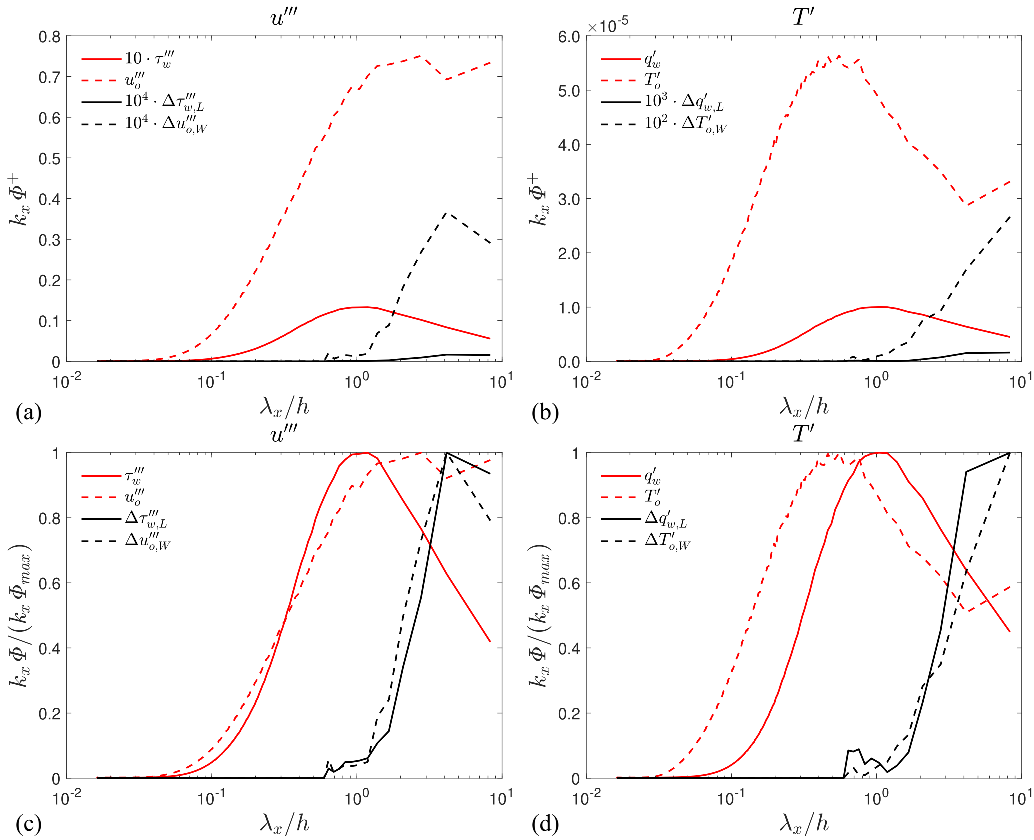

FIG. 8. Comparison of premultiplied energy spectra of the original field and the attached eddies at a given scale in both the streamwise velocity u''' and temperature T' fluctuations of case M15R20K in the near-wall region and logarithmic region ($y^* = 200$), where τ'''_w and q'_w are the wall shear stress and wall heat flux, respectively. (a) Spectra from the streamwise velocity fluctuation and (b) results from the temperature fluctuations. Note that some energy spectra in (a) and (b) are amplified by a factor given in the legend since they are too small to present. To have a closer look at the relative energy distribution, the energy spectra are normalized by their maximum: (c) those from the streamwise velocity fluctuation; (d) those from the temperature fluctuations.

energy distribution, the normalized spectra by their maximum are also displayed in Figs. 8(c) and 8(d). The original ones in the near-wall and logarithmic regions have an apparently distinct energy distribution. As for those of a given scale, they share a similar energy distribution. It is worth mentioning that the contribution of VLSMs is not fully eliminated in the present scale-separation procedure, mainly due to the low Reynolds-number effects and limited computational domain of the available DNS data set. Nevertheless, one can conclude that the signature of attached eddies at a given scale has been well identified and isolated.

C. Conditional statistics of attached eddies

Apart from the spectrum features, this section gives more statistics of the attached eddy signature extracted by SLSE, including the logarithmic decay property of the variance of the streamwise velocity $\overline{u'''_{o,W}{}^2}^+$ and the root-mean square (rms) of temperature fluctuations ${T'_{o,W,rms}}^+$, and the autocorrelation function of attached eddy signatures from a certain scale in both the u''' and T' fields,

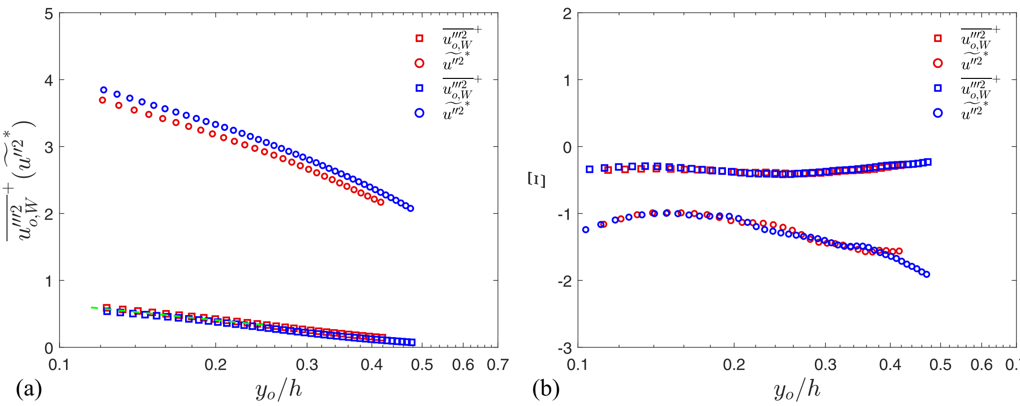

FIG. 9. (a) Normal Reynolds stress $\widetilde{u''^2}^*$ and $\overline{u'''^2_{o,W}}^+$ vs y_o/h; (b) indicator Ξ defined in Eq. (19) evaluating the logarithmic dependence of $\widetilde{u''^2}^*$ and $\overline{u'''^2_{o,W}}^+$ on y_o/h. The green dotted lines present a linear fit of $\overline{u'''^2_{o,W}}^+$ vs y_o/h as a function of y_o/h, which has a slope of approximately 0.34. The red scatters present the results of case M08R17K, and the blue ones present those of case M15R20K.

i.e., $R_{\triangle u'''_{o,W}\triangle u'''_{o,W}}$ and $R_{\triangle T'_{o,W}\triangle T'_{o,W}}$, and the characteristic scale of attached eddy determined through the autocorrelation function.

One generally interesting characteristic of attached eddies is the logarithmic decay of the normal Reynolds stress $\widetilde{u''^2}^*$ on y_o/h [4], namely,

$$\widetilde{u''^2}^* = C_2 - C_1 \ln(y_o/h), \tag{18}$$

which can be characterized by an indicator Ξ defined by

$$\Xi = y(\partial \widetilde{u''^2}^* / \partial y), \tag{19}$$

where C_1 and C_2 are constants, and C_1 is dubbed the Townsend-Perry constant. It is obvious that the indicator $\Xi = -C_1$ if the logarithmic behavior of $\widetilde{u''^2}^*$ exists. The logarithmic behavior is also expected for the estimated wall-coherent portion of normal Reynolds stress $\overline{u'''^2_{o,W}}^+$, since this portion is contributed by attached eddies [20,44]. This work scrutinizes the variation of both the original normal Reynolds stress $\widetilde{u''^2}^*$ and the estimated wall-coherent portion $\overline{u'''^2_{o,W}}^+$ with respect to y_o/h as displayed in Fig. 9(a), and Fig. 9(b) shows their corresponding indicators versus y_o/h for cases M08R17K and M15R20K. A more clear logarithmic dependence can be seen as highlighted by green dashed lines and implied by the plateau in Figs. 9(a) and 9(b), respectively. Regarding $\overline{u'''^2_{o,W}}^+$, these two cases share a common slope C_1 about 0.34, which is smaller than the Townsend-Perry constant 1.26 and 0.98 reported by Baars and Marusic [44]. On the contrary, the original normal Reynolds stress $\widetilde{u''^2}^*$ has a C_1 of approximately 1, which is closer to the Townsend-Perry constant [44]. Cheng *et al.* [20] attribute this difference mainly to the effects of VLSMs. Here we provide another explanation and ascribe these gentle slopes mainly to the more predominant role of the near-wall universal signal for low-Reynolds-number cases while applying SLSE. As discussed in Appendix B, the practically estimated $U_{o,W}(\lambda_x)$ has an energy density $|U_{o,W}(\lambda_x)|^2 = |U'_{o,W}(\lambda_x)|^2/[1 + c(\lambda_x)]$ given by Eq. (B4). This relation shows that the practically estimated energy density is smaller than the ideal one, and the difference between the practical and ideal one relies on the energy ratio $c(\lambda_x) = |U_{i,un}(\lambda_x)|^2/|U_{i,fp}(\lambda_x)|^2$. With the increase of the Reynolds number, more attached eddies appear in the logarithmic region, leading to a smaller $c(\lambda_x)$. Consequently, higher Reynolds-number cases are supposed to have a decay rate representative of the real one. In this work, $c(\lambda_x)$ could be 2–3 as the highest LCF between the inner and outer region

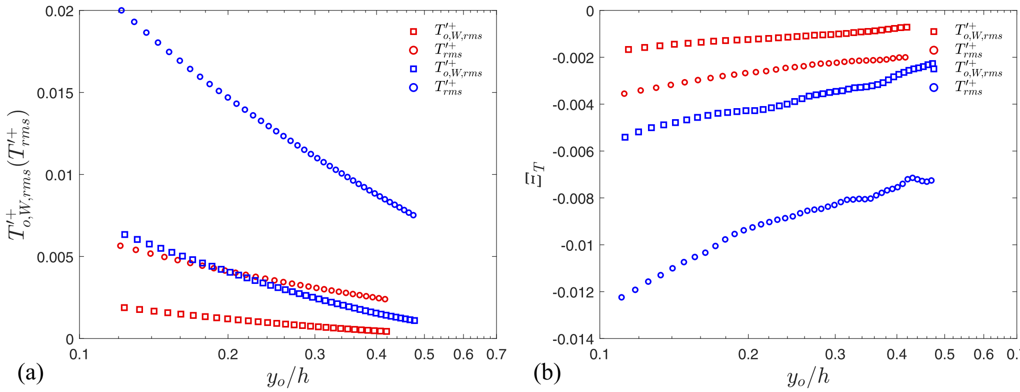

FIG. 10. (a) RMS of temperature fluctuations T'^{+}_{rms} and ${T'_{o,W,rms}}^{+}$ vs y_o/h; (b) the indicator Ξ_T following Eq. (19) with $\widetilde{u''^2}^{*}$ replaced by T'^{+}_{rms} or ${T'_{o,W,rms}}^{+}$ evaluating their logarithmic dependence on y_o/h. The red scatters present the results of case M08R17K, and the blue ones present those of case M15R20K.

is around 0.3. Note that the gentler decay rate is a combined effect of all the wavelengths, but the discussion here mainly focusing on a specific wavelength is capable of providing an intuitive explanation. This explanation also clarifies the reason why a significant discrepancy of C_1 is noticed for cases with different Reynolds numbers [20,44] even though a similar method is applied to extract the contribution from attached eddies. It merits noting that both the two factors proposed by Cheng *et al.* [20], and this work could work together to result in different decay rates.

Similarly to the streamwise velocity, temperature, which tends to exhibit a logarithmic decay with increasing Reynolds numbers, is also an attached variable [24]. Figure 10(a) presents the rms of original temperature fluctuations T'^{+}_{rms} and its wall-attached portion ${T'_{o,W,rms}}^{+}$ with respect to the outer-scaled wall-normal distance y_o/h, and Fig. 10(b) provides the corresponding indicator function Ξ_T that shares a similar definition given by Eq. (19) with $\widetilde{u''^2}^{*}$ replaced by T'^{+}_{rms} or ${T'_{o,W,rms}}^{+}$. However, it is difficult to distinguish a logarithmic distribution from both the temperature fluctuation itself and its wall-attached portion. No plateau appears in Fig. 10(b) though ${T'_{o,W,rms}}^{+}$ has a flatter indicator function, which further evidences this observation. The relatively lower Reynolds number of the current database could be blamed for the unsatisfactory performance of the original temperature fluctuation. The wall-attached portion ${T'_{o,W,rms}}^{+}$ is more characterized by the AEH [4] compared with the original T'^{+}_{rms} because of its less sharp Ξ_T. Unfortunately, due to limitations of the current framework discussed in Appendix B, the "noise" in the near-wall region can not be eliminated and results in the blurred logarithmic distribution.

The autocorrelation functions of $R_{\triangle u'''_{o,W}\triangle u'''_{o,W}}$ and $R_{\triangle T'_{o,W}\triangle T'_{o,W}}$ are displayed in Figs. 11 and 12(a) separately to demonstrate the scale of structures. As the current isolation methodology recognizes $\triangle u'''_{o,W}(\triangle T'_{o,W})$ as signatures of attached eddies of a uniform size, the autocorrelation function $R_{\triangle u'''_{o,W}\triangle u'''_{o,W}}(R_{\triangle T'_{o,W}\triangle T'_{o,W}})$ is supposed to represent the features of uniformly sized eddies. The curvature of the correlation functions in Figs. 11 and 12(a) is nowhere large compared with the common high curvature of $R_{u'''u'''}$ (not shown) near $\triangle x = 0$, which indicates the signature from eddies of a similar size [4]. To quantify the size growth of eddies, we characterize the eddy size by $\triangle x^*_{0.05}$ the streamwise shift corresponding to $R_{\triangle u'''_{o,W}\triangle u'''_{o,W}(R_{\triangle T'_{o,W}\triangle T'_{o,W}})} = 0.05$ as shown in Figs. 11 and 12(b). The AEH [4] claims that the attached eddy scale is linearly proportional to its height, i.e., the wall-normal distance. Therefore, a linear fit is applied to $\triangle x^*_{0.05}$ obtained in u''' and T' fields, and the result is superposed onto Figs. 11 and 12(b) by the black dashed and dotted lines. In Fig. 11(b), $\triangle x^*_{0.05}$ from case M08R17K coincides well with $\triangle x^*_{0.05} = 7.8 \cdot y^*_m$, and so does case M15R20K for $y/h < 0.2$. The slope 7.8 is consistent with the streamwise/wall-normal aspect ratio 14 in incompressible flows [32] and the slightly higher value around 15 computed through LCF

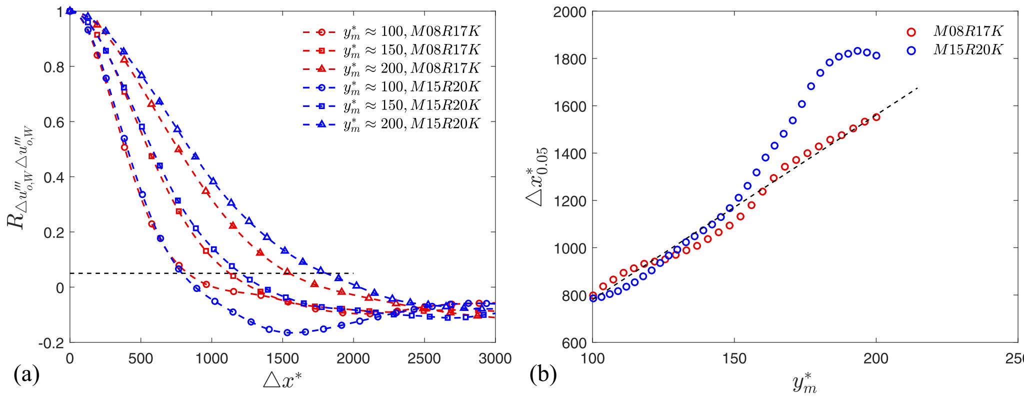

FIG. 11. (a) Autocorrelation coefficient $R_{\triangle u'''_{o,W} \triangle u'''_{o,W}}(\triangle x^*)$ as a function of $\triangle x^*$ at three selected wall-normal positions $y_m^* \approx 100$, 150, and 200 from cases M08R17K and M15R20K, which evaluates the scale of signatures in the logarithmic region induced by attached eddies of a given scale; the black dashed line in (a) denotes $R_{\triangle u'''_{o,W} \triangle u'''_{o,W}} = 0.05$. (b) $\triangle x^*_{0.05}$ where $R_{\triangle u'''_{o,W} \triangle u'''_{o,W}}(\triangle x^*_{0.05}) \approx 0.05$ with respect to y_m^*. The black dashed line in (b) is $\triangle x^*_{0.05} = 7.8 \cdot y_m^*$.

in Sec. IV A, because the axisymmetric property of the autocorrelation function leads to the actual size of eddies to be around $2\triangle x^*_{0.05}$. On the contrary, $\triangle x^*_{0.05}$ of T' fields shows less agreement than that of u''' fields. Figure 12(b) indicates that the scale of eddies in T' is generally larger due to the influence of VLSMs and fluctuates more. They can roughly be characterized by lines with slopes of 3.9 and 5.6 for cases M08R17K and M15R20K and nonzero intersection with $y_m^* = 0$, respectively. Although their increasing rate is slower than the expected value of around 7, it is acceptable to present the linear increase of the characteristic scale. In a word, the examination of the attached eddy scale versus the wall-normal distance demonstrates the capability of the present technique to isolate signatures from attached eddies of a certain scale in both the velocity and temperature fields.

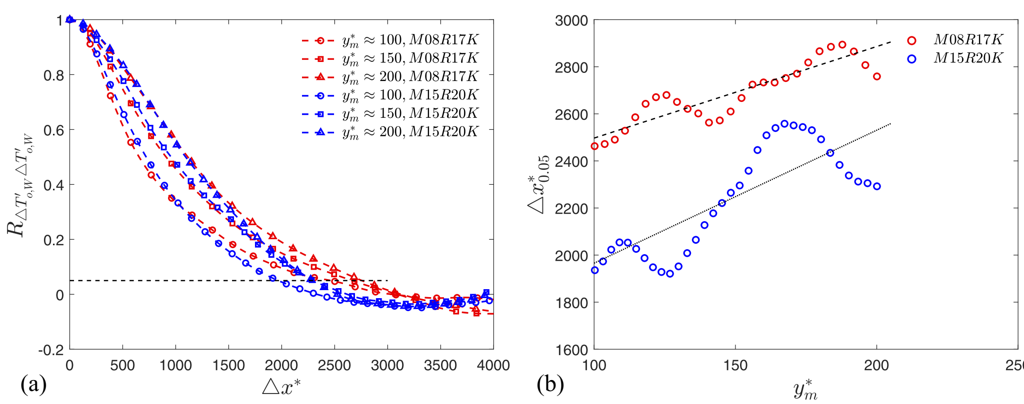

FIG. 12. (a) Autocorrelation coefficient $R_{\triangle T'_{o,W} \triangle T'_{o,W}}(\triangle x^*)$ as a function of $\triangle x^*$ at three selected wall-normal positions $y_m^* \approx 100$, 150, and 200 from cases M08R17K and M15R20K, which evaluates the scale of signatures in the logarithmic region induced by attached eddies of a given scale; the black dashed line in (a) denotes $R_{\triangle T'_{o,W} \triangle T'_{o,W}} = 0.05$. (b) $\triangle x^*_{0.05}$ where $R_{\triangle T'_{o,W} \triangle T'_{o,W}}(\triangle x^*_{0.05}) \approx 0.05$ with respect to y_m^*. The black dashed line in (b) has a slope of 3.9, and the black dotted line has a slope of 5.6.

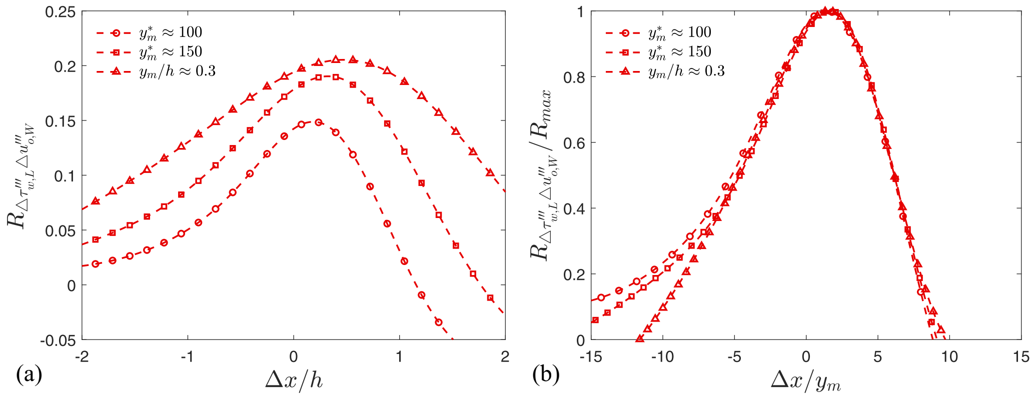

FIG. 13. (a) Cross-correlation coefficient $R_{\triangle\tau'''_{w,L}\triangle u'''_{o,W}}$ as a function of $\triangle x/h$ at three selected wall-normal positions $y_m^* \approx 100$, 150, and $y_m/h = 0.3$ from case M15R20K, which evaluates the correlation between wall shear stress and signatures in the logarithmic region induced by attached eddies of a given scale. (b) Normalized $R_{\triangle\tau'''_{w,L}\triangle u'''_{o,W}}$ by its maximum $R_{\max} = \max(R_{\triangle\tau'''_{w,L}\triangle u'''_{o,W}})$ and wall-normal distance y_m at the same positions from the same case.

D. The Mach-number effect on the streamwise inclination angle

This section shows the Mach-number influence for both the mean inclination angle α_m and that of attached eddies at a given height α_s using compressible turbulent channel flows up to $\mathrm{Ma}_b = 3$, the highest Ma_b we can achieve currently because of the unaffordable cost for higher Mach numbers. The mean streamwise inclination angle α_m for u''' and T' as a function of the wall-normal distance y^* is plotted, and α_s for u''' and T' versus their height y_m^* is plotted as well. A comparison between them is conducted to demonstrate the ensemble influence of multiscale attached eddies. To better demonstrate the Mach-number effect, we present the average value of α_s over the logarithmic region, and a comparison is conducted with the incompressible flows [20], indicative of the Reynolds-number effect.

The cross-correlations between the wall shear stress/heat flux fluctuation and signatures in the logarithmic region induced by attached eddies of a given scale in both the streamwise velocity and temperature fluctuations are shown in Figs. 13 and 14, respectively. These correlations are

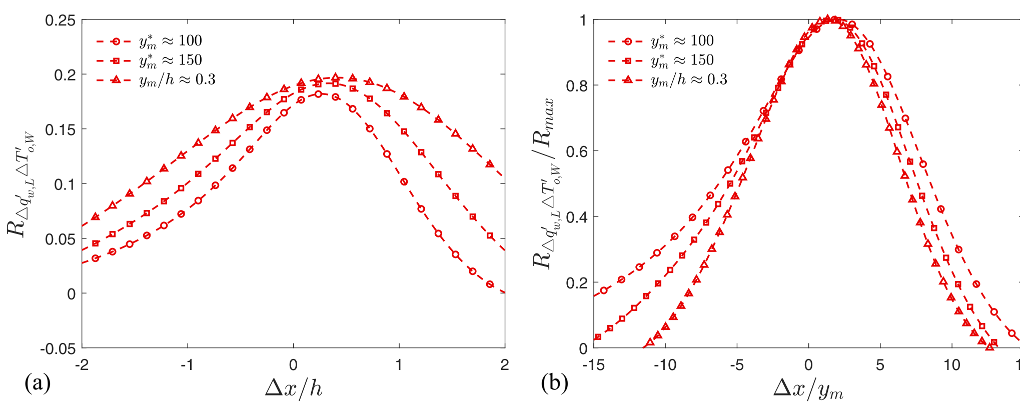

FIG. 14. (a) Cross-correlation coefficient $R_{\triangle q'_{w,L}\triangle T'_{o,W}}$ as a function of $\triangle x/h$ at three selected wall-normal positions $y_m^* \approx 100$, 150, and $y_m/h = 0.3$ from case M15R20K. (b) Normalized $R_{\triangle q'_{w,L}\triangle T'_{o,W}}$ by its maximum $R_{\max} = \max(R_{\triangle q'_{w,L}\triangle T'_{o,W}})$ and wall-normal distance y_m at the same positions from the same case.

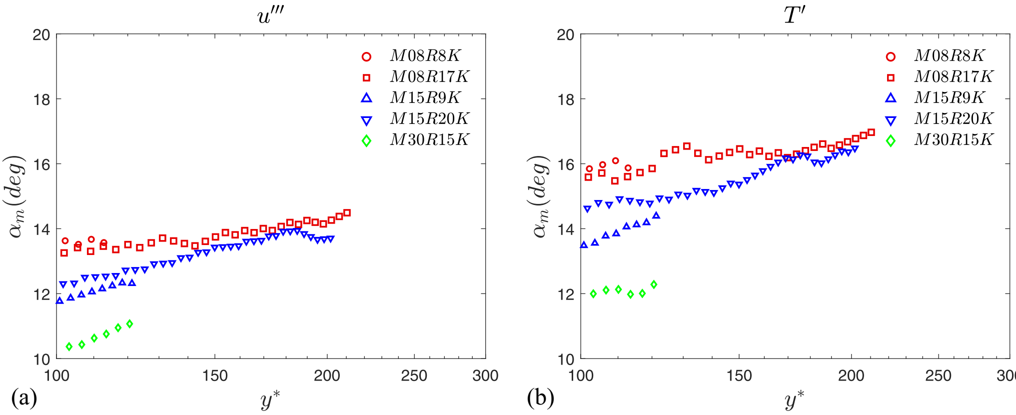

FIG. 15. Streamwise inclination angle α_m of wall-attached eddies under the assemble effect of multiscale eddies versus the wall-normal location y^* where the inclination angle is evaluated in both the streamwise velocity u''' and temperature T' using the DNS database in Table I. (a) Results from the streamwise velocity fluctuation; (b) those from the temperature fluctuations.

computed from case M15R20K and employed to determine the streamwise inclination angle through the streamwise offset corresponding to the peak correlation. A better collapse of normalized cross-correlation coefficients is noticed in Figs. 13(b) and 14(b), especially for streamwise velocity fluctuations. However, it disappears if one uses the traditional cross-correlation $R_{\tau'_w u'}$, which is not shown here for brevity. This observation indicates that the self-similar characteristics of the energy-containing motions in the logarithmic region are captured by the current scale-separation method.

In Fig. 15, α_m is 10°–15° for velocity fluctuations and 12°–17° for temperature fluctuations in all the four cases. The average inclination angle α_m, which has been shown to be Reynolds-number invariant [18], remains approximately comparable for different Mach numbers in this work. The mean inclination angle of u''' we obtained here is close to the u-bearing structure angle in Pirozzoli and Bernardini [24] in the outer layer, although the structure angle defined in [24] is not necessarily the inclination angle of attached eddies. Instead, it can be considered as a characteristic angle of u-bearing eddies centered at the reference wall distance $\bar{y}$. However, the α_m of T' is much smaller than that in Pirozzoli and Bernardini [24] since the α_m of T' is comparable to that of u'''. Pirozzoli and Bernardini [24] ascribe this difference to the more passive dynamics of the temperature field than the velocity field. If one considers the consistent inclination angle of the velocity field from two different methods, the more passive role of temperature is very likely to be one crucial contributor to the discrepancy between the current one and that in the previous work [24]. It is worth mentioning that the structure angle in Pirozzoli and Bernardini [24] shares the same ensemble feature from multiscale eddies as α_m. Obviously, it is too complicated to provide an explanation for the comparison with α_s explicitly due to the influence of multiple factors. We retain its comparison with α_m only.

In Fig. 16 the inclination angle of streamwise velocity u''' varies slightly over the logarithmic region, while that of temperature T' fluctuates more near the outer edge of the logarithmic region. The average value of α_s may represent its features as shown in Fig. 17, where four extra results [20] from incompressible channel flows with Re_τ ranging from 550 to 4000 are superposed for reference. The average values $\alpha_{s,m}$ in u''' fields displayed in Fig. 17 are 24°, 30°, 23°, 32°, and 24° for M08R8K, M08R17K, M15R9K, M15R20K, and M30R15K correspondingly for four cases. For compressible wall-bounded turbulence, we follow Morkovin's hypothesis [41] and use the semilocal friction Reynolds number Re_τ^* to characterize the channel flows instead of Re_τ adopted in the incompressible regime. It is noticed that cases M08R8K, M15R9K, and M30R15K share a comparable Re_τ^*, and

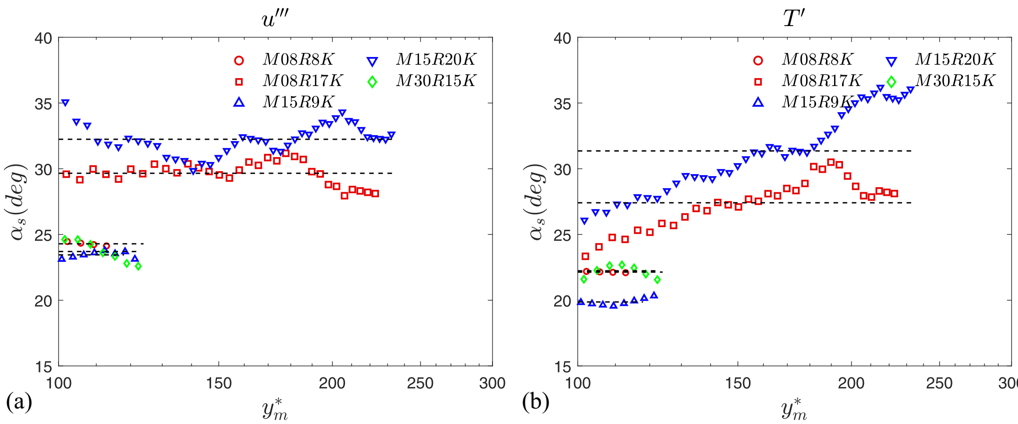

FIG. 16. Streamwise inclination angle α_s of wall-attached eddies at a given height vs their height y_m^* in both the streamwise velocity u''' and temperature T' using the DNS database in Table I. (a) Results from the streamwise velocity fluctuation; (b) those from the temperature fluctuations. The black dashed lines indicate the average value of each case in the logarithmic region.

their average α_s is close to each other as well. Similarly, the analogy between cases M08R17K and M15R20K also exists. More importantly, these five $\alpha_{s,m}$ obtained in compressible channel flows are consistent with the asymptotic curve (the black dashed line in Fig. 17) predicted by $\alpha_{s,m}$ from incompressible channel flows [20] if one considers their semilocal friction Reynolds number

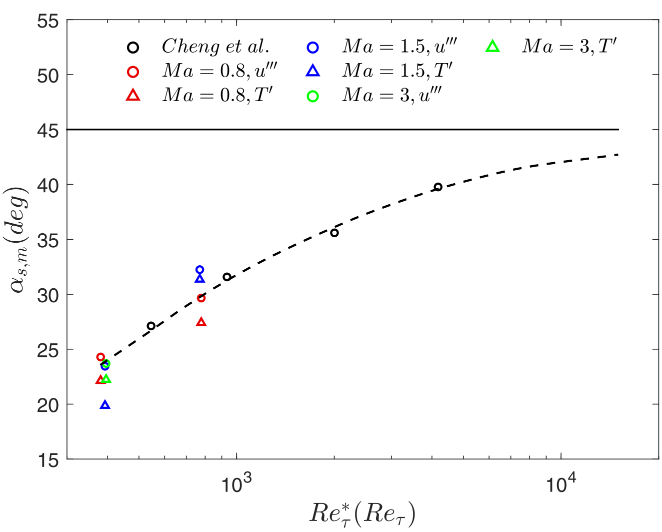

FIG. 17. Variation of average values $\alpha_{s,m}$ of the streamwise inclination angle of wall-attached eddies at a given scale with Reynolds numbers $\mathrm{Re}_\tau^*(\mathrm{Re}_\tau)$ in both the streamwise velocity u''' and temperature T' using the DNS database in Table I. The corresponding results from incompressible flows computed in Cheng *et al.* [20] are also included for reference, which are denoted by black circles. From lower to higher average inclination angles, these four black circles are from incompressible channel flows at $\mathrm{Re}_\tau \approx 547$ [46], 934 [47], 2003 [48], and 4179 [49]. The black solid line is the theoretical prediction angle 45°, and the black dashed line denotes the asymptotic performance of $\alpha_{s,m}$ computed from incompressible flows.

Re_τ^*. This inspection further gauges the validity of Morkovin's hypothesis [41]. Cheng *et al.* [20] notice that α_s of an incompressible channel flow at $\mathrm{Re}_\tau = 550$ is around 27° and 31° for a case at $\mathrm{Re}_\tau = 950$. These two cases in Cheng *et al.* [20] are analogous to cases used in this work, and the agreement between the incompressible and compressible cases at similar semilocal friction Reynolds numbers can be clearly confirmed. Therefore, an increasing trend of α_s with Reynolds numbers as indicated by the black dashed line [20] is much more distinct than that of Mach numbers, and α_s can be considered a Mach-number independent parameter for the present considered DNS database. This negligible Mach-number impact on α_s plays an important role in the AEH [4], which allows us to extend it to compressible flows directly once we obtain its semilocal friction Reynolds number, and build a uniform model for cases with different Mach numbers. Figure 17 also plots $\alpha_{s,m}$ in temperature fluctuations T'. The $\alpha_{s,m}$ are 22°, 27°, 20°, 31°, and 22° for M08R8K, M08R17K, M15R9K, M15R20K, and M30R15K correspondingly, which are comparable to those obtained in u''' fields of both compressible and incompressible flows. Unsurprisingly, an analogous α_s between streamwise velocity and temperature fluctuations appears due to the validity of SRA [24,43,45]. Again, α_s of temperature fluctuations T' depends less on the Mach number for the present DNS database.

In summary, both α_s and α_m show independence on the Mach number for the five cases checked in the current work. While α_m is also Reynolds number invariant, α_s approaches 45° as the Reynolds number increases.

V. CONCLUDING REMARKS

This work uses DNS results of compressible channel flows over a broad range of Reynolds and Mach numbers to investigate the streamwise inclination angle of wall-attached eddies of a given scale. The SLSE is adopted to extract the signature of attached eddies in the near-wall and logarithmic regions. Another streamwise angle α_{hl} (13°–20° following the feature of attached eddies) defined based on the maximum weighting in the impulse response function shows in the physical space that coherent structures extracted by SLSE are typically attached eddies. Then it is followed by a subtraction between two adjacent wall-normal locations to isolate the signature contributed by eddies of a given scale. Through computing the cross-correlation of signatures in the near-wall and logarithmic regions, the streamwise inclination angle for attached eddies of a given height is obtained. This streamwise inclination angle approaches 45° asymptotically as the Reynolds number increases, while the Mach number has a minor influence on it, based on the available DNS data. For those results in temperature-fluctuating fields, high statistical similarity to the streamwise velocity fluctuations is observed, and the corresponding streamwise inclination angle also depends more on the Reynolds numbers. This conclusion allows a uniform model to be applied to cases with different Mach numbers and comparable Reynolds numbers.

The data that support the findings of this study are available on request from the corresponding author.

ACKNOWLEDGMENTS

L.F. acknowledges the fund from the Research Grants Council (RGC) of the Government of Hong Kong Special Administrative Region (HKSAR) with RGC/ECS Project (No. 26200222), RGC/GRF Project (No. 16201023), and RGC/STG Project (No. STG2/E-605/23-N), the fund from the Guangdong Basic and Applied Basic Research Foundation, the fund from the Guangdong Province Science and Technology Plan Project (No. 2023A0505030005), the fund from the Center for Ocean Research in Hong Kong and Macau, a joint research center between Laoshan Laboratory and HKUST, and the fund from the Project of Hetao Shenzhen–Hong Kong Science and Technology Innovation Cooperation Zone (No. HZQB-KCZYB-2020083).

The authors report no conflict of interest.

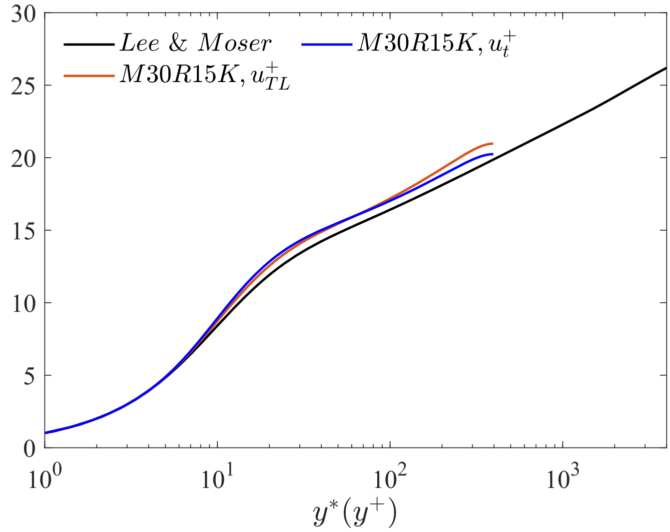

FIG. 18. Mean streamwise velocity profiles transformed by the Trettel-Larsson transformation [50] and the total-stress-based transformation [51]. The black solid line denotes the reference, which is taken from the incompressible channel flow with $\mathrm{Re}_\tau \approx 5200$ by [52].

APPENDIX A: VALIDATION OF THE DNS AT $\mathrm{Ma}_b = 3$

The accuracy of the DNS case at $\mathrm{Ma}_b = 3$ is validated through the mean streamwise velocity profile. A velocity transformation is required to account for the compressibility effect to recover the incompressible law of the wall. This work utilizes the Trettel-Larsson [50] and total-stress-based [51] transformations which perform well in compressible channel flows. The transformed velocity profiles shown in Fig. 18 both have a satisfactory collapse to the well-known law of the wall.

APPENDIX B: SLSE WITH UNCORRELATED INPUT NOISES

This work uses fluctuation fields as the input signal of SLSE. However, these inputs all have contributions not from attached eddies, which are recognized as noises in this work [35]. The near-wall signals consist of both the footprint and universe signals, and the outer-region signals contain the attached and detached portions. In this Appendix we discuss the influence of these uncorrelated noises on SLSE using an example the near-wall velocity signal as the input. Neglecting the modulation process of IOIM [22], the near-wall signal can be expressed by $u_i''' = u_{i,fp}''' + u_{i,un}'''$, where $u_{i,fp}'''$ is the footprint of attached eddies, $u_{i,un}'''$ is the universal signal, and $u_{i,un}'''$ is assumed to be uncorrelated with $u_{i,fp}'''$ and u_o'''.

In the ideal situation, the estimated outer signal $U_{o,W}'(\lambda_x)$ is given by $H_W'(\lambda_x)U_{i,fp}(\lambda_x)$, where $H_W'(\lambda_x) = \langle\overline{U_{i,fp}(\lambda_x)}U_o(\lambda_x)\rangle/\langle|U_{i,fp}(\lambda_x)|^2\rangle$ is the exact transfer kernel for the interaction process between the inner and outer region. However, the practical SLSE process conducts it by $U_{o,W}(\lambda_x) = H_W(\lambda_x)[U_{i,fp}(\lambda_x) + U_{i,un}(\lambda_x)]$, where $U_{i,fp}(\lambda_x) = F(u_{i,fp}'''(x))$ and $U_{i,un}(\lambda_x) = F(u_{i,un}'''(x))$. One can immediately derive the relation between the exact transfer kernel $H_W'(\lambda_x)$ and the practical transfer kernel $H_W(\lambda_x)$:

$$H_W(\lambda_x) = \frac{\langle\overline{U_i(\lambda_x)}U_o(\lambda_x)\rangle}{|U_i(\lambda_x)|^2} = \frac{\langle\overline{U_{i,fp}(\lambda_x)}U_o(\lambda_x)\rangle}{|U_{i,fp}(\lambda_x)|^2 + |U_{i,un}(\lambda_x)|^2} = \frac{H_W'(\lambda_x)}{1 + c(\lambda_x)}, \tag{B1}$$

where $c(\lambda_x) = |U_{i,un}(\lambda_x)|^2/|U_{i,fp}(\lambda_x)|^2$ is the energy ratio between the universal signal and the footprint at each wavelength. Thus, the practical kernel is an optimum approximation of the exact one.

With the relation between $H'_W(\lambda_x)$ and $H_W(\lambda_x)$, $U_{o,W}(\lambda_x)$ can be expressed by

$$U_{o,W}(\lambda_x) = \frac{H'_W(\lambda_x)}{1+c(\lambda_x)}[U_{i,fp}(\lambda_x) + U_{i,un}(\lambda_x)]. \tag{B2}$$

The energy contained in each wavelength is also of interest. As for the ideal case, it is easy to obtain

$$|U'_{o,W}(\lambda_x)|^2 = |H'_W(\lambda_x)|^2|U_{i,fp}(\lambda_x)|^2. \tag{B3}$$

Those of $U_{o,W}(\lambda_x)$ can be manipulated into a function of $|U'_{o,W}(\lambda_x)|^2$. The derivation goes as follows:

$$\begin{aligned}
|U_{o,W}(\lambda_x)|^2 &= |H_W(\lambda_x)|^2|U_{i,fp}(\lambda_x) + U_{i,un}(\lambda_x)|^2 \\
&= \frac{|H'_W(\lambda_x)|^2}{[1+c(\lambda_x)]^2}[|U_{i,fp}(\lambda_x)|^2 + |U_{i,un}(\lambda_x)|^2] \\
&= \frac{|H'_W(\lambda_x)|^2}{[1+c(\lambda_x)]^2}[1+c(\lambda_x)]|U_{i,fp}(\lambda_x)|^2 \\
&= \frac{|H'_W(\lambda_x)|^2}{1+c(\lambda_x)}|U_{i,fp}(\lambda_x)|^2 \\
&= \frac{|U'_{o,W}(\lambda_x)|^2}{1+c(\lambda_x)}.
\end{aligned} \tag{B4}$$

These relations between $H'_W(\lambda_x)$ and $H_W(\lambda_x)$ and between $|U_{o,W}(\lambda_x)|^2$ and $|U'_{o,W}(\lambda_x)|^2$ are powerful tools to explain observations in this paper, which will be frequently accessed by the main text. The authors also prefer to point out that the current framework is not able to exactly identify $c(\lambda_x)$ and give accurate predictions.

[1] C. R. Smith, J. D. A. Walker, A. H. Haidari, and U. Sobrun, On the dynamics of near-wall turbulence, Philos. Trans. R. Soc. London A **336**, 131 (1991).

[2] B. Green, *Fluid Vortices* (Kluwer Academic Publishers, Dordrecht, the Netherlands, 1995).

[3] R. J. Adrian, Hairpin vortex organization in wall turbulence, Phys. Fluids **19**, 041301 (2007).

[4] A. Townsend, *The Structure of Turbulent Shear Flow* (Cambridge University Press, Cambridge, UK, 1976).

[5] A. E. Perry and M. S. Chong, On the mechanism of wall turbulence, J. Fluid Mech. **119**, 173 (1982).

[6] A. Perry, S. Henbest, and M. Chong, A theoretical and experimental study of wall turbulence, J. Fluid Mech. **165**, 163 (1986).

[7] C. Meneveau and I. Marusic, Generalized logarithmic law for high-order moments in turbulent boundary layers, J. Fluid Mech. **719**, R1 (2013).

[8] A. Perry and I. Marušić, A wall-wake model for the turbulence structure of boundary layers. Part 1. Extension of the attached eddy hypothesis, J. Fluid Mech. **298**, 361 (1995).

[9] I. Marušić and A. Perry, A wall-wake model for the turbulence structure of boundary layers. Part 2. Further experimental support, J. Fluid Mech. **298**, 389 (1995).

[10] I. Marusic, On the role of large-scale structures in wall turbulence, Phys. Fluids **13**, 735 (2001).

[11] I. Marusic and J. P. Monty, Attached eddy model of wall turbulence, Annu. Rev. Fluid Mech. **51**, 49 (2019).

[12] C. Cheng, W. Li, A. Lozano-Durán, and H. Liu, Identity of attached eddies in turbulent channel flows with bidimensional empirical mode decomposition, J. Fluid Mech. **870**, 1037 (2019).
[13] S. K. Robinson, Coherent motions in the turbulent boundary layer, Annu. Rev. Fluid Mech. **23**, 601 (1991).
[14] M. Head and P. Bandyopadhyay, New aspects of turbulent boundary-layer structure, J. Fluid Mech. **107**, 297 (1981).
[15] R. J. Adrian, C. D. Meinhart, and C. D. Tomkins, Vortex organization in the outer region of the turbulent boundary layer, J. Fluid Mech. **422**, 1 (2000).
[16] P. Moin and J. Kim, The structure of the vorticity field in turbulent channel flow. Part 1. Analysis of instantaneous fields and statistical correlations, J. Fluid Mech. **155**, 441 (1985).
[17] A. E. Perry, A. K. M. Uddin, and I. Marusic, An experimental and computational study on the orientation of attached eddies in turbulent boundary layers, in *Proceedings of the 11th Australasian Fluid Mechanics Conference, University of Tasmania, Hobart, Australia* (1992).
[18] I. Marusic and W. D. Heuer, Reynolds number invariance of the structure inclination angle in wall turbulence, Phys. Rev. Lett. **99**, 114504 (2007).
[19] R. Deshpande, J. P. Monty, and I. Marusic, Streamwise inclination angle of large wall-attached structures in turbulent boundary layers, J. Fluid Mech. **877**, R4 (2019).
[20] C. Cheng, W. Shyy, and L. Fu, Streamwise inclination angle of wall-attached eddies in turbulent channel flows, J. Fluid Mech. **946**, A49 (2022).
[21] R. Baidya, W. Baars, S. Zimmerman, M. Samie, R. J. Hearst, E. Dogan, L. Mascotelli, X. Zheng, G. Bellani, A. Talamelli *et al.*, Simultaneous skin friction and velocity measurements in high Reynolds number pipe and boundary layer flows, J. Fluid Mech. **871**, 377 (2019).
[22] I. Marusic, R. Mathis, and N. Hutchins, Predictive model for wall-bounded turbulent flow, Science **329**, 193 (2010).
[23] L. Duan, I. Beekman, and M. Martin, Direct numerical simulation of hypersonic turbulent boundary layers. Part 3. Effect of Mach number, J. Fluid Mech. **672**, 245 (2011).
[24] S. Pirozzoli and M. Bernardini, Turbulence in supersonic boundary layers at moderate Reynolds number, J. Fluid Mech. **688**, 120 (2011).
[25] A. J. Smits, B. J. McKeon, and I. Marusic, High–Reynolds number wall turbulence, Annu. Rev. Fluid Mech. **43**, 353 (2011).
[26] E. F. Spina, A. J. Smits, and S. K. Robinson, The physics of supersonic turbulent boundary layers, Annu. Rev. Fluid Mech. **26**, 287 (1994).
[27] A. J. Smits and J.-P. Dussauge, *Turbulent Shear Layers in Supersonic Flow* (Springer Science & Business Media, New York, 2006).
[28] B. Ganapathisubramani, N. Clemens, and D. Dolling, Large-scale motions in a supersonic turbulent boundary layer, J. Fluid Mech. **556**, 271 (2006).
[29] X. Chen, C. Cheng, J. Gan, and L. Fu, Study of the linear models in estimating coherent velocity and temperature structures for compressible turbulent channel flows, J. Fluid Mech. **973**, A36 (2023).
[30] M. Yu, C. Xu, J. Chen, P. Liu, Y. Fu, and X. Yuan, Spectral decomposition of wall-attached/detached eddies in compressible and incompressible turbulent channel flows, Phys. Rev. Fluids **7**, 054607 (2022).
[31] C. Cheng and L. Fu, Large-scale motions and self-similar structures in compressible turbulent channel flows, Phys. Rev. Fluids **7**, 114604 (2022).
[32] W. J. Baars, N. Hutchins, and I. Marusic, Self-similarity of wall-attached turbulence in boundary layers, J. Fluid Mech. **823**, R2 (2017).
[33] K. P. Griffin, L. Fu, and P. Moin, Near-wall model for compressible turbulent boundary layers based on an inverse velocity transformation, J. Fluid Mech. **970**, A36 (2023).
[34] C. Cheng, X. Chen, W. Zhu, W. Shyy, and L. Fu, Progress in physical modeling of compressible wall-bounded turbulent flows, Acta Mech. Sin. **40**, 323663 (2024).
[35] J. S. Bendat and A. G. Piersol, *Random Data: Analysis and Measurement Procedures* (John Wiley & Sons, 2011).
[36] C. Tinney, F. Coiffet, J. Delville, A. Hall, P. Jordan, and M. Glauser, On spectral linear stochastic estimation, Exp. Fluids **41**, 763 (2006).

[37] W. J. Baars, N. Hutchins, and I. Marusic, Spectral stochastic estimation of high-Reynolds-number wall-bounded turbulence for a refined inner-outer interaction model, Phys. Rev. Fluids **1**, 054406 (2016).

[38] C. Cheng and L. Fu, Consistency between the attached-eddy model and the inner–outer interaction model: A study of streamwise wall-shear stress fluctuations in a turbulent channel flow, J. Fluid Mech. **942**, R9 (2022).

[39] C. Cheng and L. Fu, Linear-model-based study of the coupling between velocity and temperature fields in compressible turbulent channel flows, J. Fluid Mech. **964**, A15 (2023).

[40] C. Cheng and L. Fu, A scale-based study of the Reynolds number scaling for the near-wall streamwise turbulence intensity in wall turbulence, Int. J. Heat Fluid Flow **101**, 109136 (2023).

[41] M. V. Morkovin, Effects of compressibility on turbulent flows, in *Méchanique de la Turbulence*, edited by A. Favre (CNRS, Paris, 1962). pp. 367–380.

[42] P. Huang, G. N. Coleman, and P. Bradshaw, Compressible turbulent channel flows: DNS results and modelling, J. Fluid Mech. **305**, 185 (1995).

[43] L. Fu, M. Karp, S. T. Bose, P. Moin, and J. Urzay, Shock-induced heating and transition to turbulence in a hypersonic boundary layer, J. Fluid Mech. **909**, A8 (2021).

[44] W. J. Baars and I. Marusic, Data-driven decomposition of the streamwise turbulence kinetic energy in boundary layers. Part 2. Integrated energy and A_1, J. Fluid Mech. **882**, A26 (2020).

[45] X. Chen, C. Cheng, L. Fu, and J. Gan, Linear response analysis of supersonic turbulent channel flows with a large parameter space, J. Fluid Mech. **962**, A7 (2023).

[46] J. C. Del Alamo and J. Jiménez, Spectra of the very large anisotropic scales in turbulent channels, Phys. Fluids **15**, L41 (2003).

[47] J. C. Del Alamo, J. Jiménez, P. Zandonade, and R. D. Moser, Scaling of the energy spectra of turbulent channels, J. Fluid Mech. **500**, 135 (1999).

[48] S. Hoyas and J. Jiménez, Scaling of the velocity fluctuations in turbulent channels up to $\mathrm{Re}_\tau = 2003$, Phys. Fluids **18**, 011702 (2006).

[49] A. Lozano-Durán and J. Jiménez, Effect of the computational domain on direct simulations of turbulent channels up to $\mathrm{Re}_\tau = 4200$, Phys. Fluids **26**, 011702 (2014).

[50] A. Trettel and J. Larsson, Mean velocity scaling for compressible wall turbulence with heat transfer, Phys. Fluids **28**, 026102 (2016).

[51] K. P. Griffin, L. Fu, and P. Moin, Velocity transformation for compressible wall-bounded turbulent flows with and without heat transfer, Proc. Natl. Acad. Sci. USA **118**, e2111144118 (2021).

[52] M. Lee and R. D. Moser, Direct numerical simulation of turbulent channel flow up to $\mathrm{Re}_\tau \approx 5200$, J. Fluid Mech. **774**, 395 (2015).